Heliyon 7 (2021) e08076

Contents lists available at ScienceDirect

Heliyon

journal homepage: www.cell.com/heliyon

Research article

Engineering Co_3O_4/MnO_2 nanocomposite materials for oxygen reduction electrocatalysis

Ababay Ketema Worku [a], Delele Worku Ayele [a,b,*], Nigus Gabbiye Habtu [a,c,**], Temesgen Atnafu Yemata [c]

[a] Bahir Dar Energy Center, Bahir Dar Institute of Technology, Bahir Dar University, Bahir Dar, P.O.BOX 26, Ethiopia
[b] Department of Chemistry, College of Science, Bahir Dar University, P.O. Box 79, Bahir Dar, Ethiopia
[c] Department of Chemical Engineering, Bahir Dar Institute of Technology, Bahir Dar University, P.O. Box 26, Bahir Dar, Ethiopia

HIGHLIGHTS

- Co_3O_4/MnO_2 nanocomposites have been effectively synthesized via a co-precipitation route.
- The addition of Co_3O_4 in MnO_2 led to a drastic change in the electrochemical properties.
- The electrochemical behaviors of Co_3O_4/MnO_2 nanocomposites have been investigated.
- The Co_3O_4/MnO_2 nanocomposite electrode exhibits high stabilities and high catalytic activities.

GRAPHICAL ABSTRACT

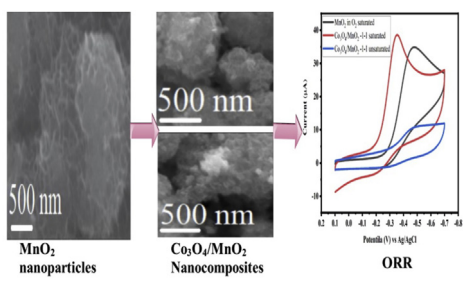

ARTICLE INFO

Keywords:
Co_3O_4/MnO_2 nanocomposite
Oxygen reduction reaction
Electrocatalysts
Co-precipitation method

ABSTRACT

Stable and active electrocatalysts preparation for the oxygen reduction reaction (ORR) is essential for an energy storage and conversion materials (e.g. metal-air batteries). Herein, we prepared a highly-active MnO_2 and Co_3O_4/MnO_2 nanocomposite electrocatalysts using a facial co-precipitation approach. The electrocatalytic activity was examined in alkaline media with LSV and CV. Additionally, the physicochemical characteristics of the MnO_2 and Co_3O_4/MnO_2 composite materials were studied via SEM, XRD, BET, UV-Vis, TGA/DTA, ICP-OES and FTIR. Morphological studies indicated that a pure MnO_2 has a spherical flower-like architecture, whereas Co_3O_4/MnO_2 nanocomposites have an aggregated needle-like structure. Moreover, from the XRD investigation parameters such as the dislocation density, micro-strain, and crystallite size were analyzed. The calculated energy bandgaps for the MnO_2, Co_3O_4/MnO_2-1-5, and Co_3O_4/MnO_2-1-1 nanocomposites were 3.07, 2.6, and 2.3 eV, correspondingly. The FTIR spectroscopy was also employed to study the presence of M-O bonds (M = Mn, Co). The thermal gravimetric investigation showed that the Co_3O_4/MnO_2 nanocomposite materials exhibited improved thermal stability, confirming an enhanced catalytic activity of ORR for MnO_2/Co_3O_4-1-1 composite materials for ORR. These results confirm that the prepared Co_3O_4/MnO_2 composite materials are promising air electrode candidates for the energy storage and conversion technologies.

* Corresponding author.
** Corresponding author.
E-mail addresses: delelewww@gmail.com (D.W. Ayele), nigushabtu@gmail.com (N.G. Habtu).

https://doi.org/10.1016/j.heliyon.2021.e08076
Received 12 May 2021; Received in revised form 7 July 2021; Accepted 23 September 2021

1. Introduction

Recently, renewable energy has been regarded as a sustainable approach to overcome current global warming issues [1, 2]. Thus, sustainable and reliable prospects can be achieved by creating novel energy conversion and storage devices [3, 4]. Thus, batteries, supercapacitors, and fuel cells are the most effective technologies for solving these challenges. The oxygen reduction reaction (ORR) is the governing electrochemical reaction in the discharge process, which affects the performance of these devices [5]. However, the ORR suffers from high polarization and sluggish kinetics, which decreases the overall performance of the battery [6, 7]. Hence, different researchers have concentrated on preparing effective, low-cost, and durable oxygen electrocatalysts to significantly enhance the reaction kinetics of the ORR. Recently, different types of electrocatalysts such as precious metals, carbon-derived catalysts, transition-metals, and transition metal oxides (e.g. NiO, CuO, MnO_2, and Co_3O_4) have been reported to overcome the overpotential and improve the cycling performance for ORR purposes [8, 9, 10]. Transition metal oxides are attractive electrocatalysts for the ORR because of their low price, remarkable cycle stability, and environmental friendliness. From them, manganese dioxide (MnO_2) has become the potential and most attractive material with best electrochemical characteristics due to its excellent specific capacity, high abundance, high specific surface area, eco-friendly, low cost, and boost catalytic activity [11, 12]. However, poor electronic conductivity is one of the opposing outcomes observed when MnO_2 is applied as an electrocatalyst owing to its limited cycle performance [13, 14]. The principal approach for enhancing the performance of MnO_2 is to blend it with conducting materials like oxides, metals, and carbon-derived materials [15, 16]. Spinel Co_3O_4 is an alternative type of electrocatalyst that has low resistivity and excellent ORR catalytic performance [17, 18]. Mixing these two classes of materials provides a nanocomposite material with collaboration and coping effects that create oxygen vacancies, which improves the ORR activity [19, 20]. To enhance the electrochemical performance of the catalysts for ORR, nanocomposite catalysts such as CuO@MnO_2 [21], $NiCo_2O_4$@MnO_2 [22], TiO_2@MnO_2 [23], ZnO/MnO_2 [24], Fe_2O_3–MnO_2 [25], Co_3O_4/MnO_2-CNTs [26], and Co_3O_4@MnO_2 [27] have been investigated. The synergetic effect of the individual components allows the nanocomposite structure to exhibit improved characteristics [28]. However, the cost-effective, novel and simple preparation route of MnO_2-based nanocomposites with excellent activity, stability, and durability remains a challenge [29, 30]. Hence, the electrochemical activity of nanocomposites depends on their preparation process because of the essential material characteristics (e.g., porosity, particle size, crystal structure, and morphology), which rely on the development of MnO_2 and Co_3O_4/MnO_2 nanocomposites [31]. Sol-gel, hydrothermal [32, 33], soft template [34, 35], micro-emulsion [36], hummers, and co-precipitation, are common techniques for the preparation of MnO_2 and Co_3O_4/MnO_2 nanocomposites. In contrast to other methods, co-precipitation preparation offers several benefits such as a simple, rapid, and cost-effective method at room temperature under ambient pressure [37]. Despite these advantages, however, studies on the co-precipitation synthesis of MnO_2 and Co_3O_4/MnO_2 nanocomposites are still limited [38, 39, 40]. Recently, nanocomposite metal oxides have gained significant attention. However, only a few studies have been conducted on Co_3O_4/MnO_2 nanocomposites as cathode materials [41, 42]. Moreover, studies on the application of Co_3O_4/MnO_2 nanocomposites as air electrodes remain limited, while the morphology and size of the synthesized materials are expected to affect their characteristics and performance. Herein we report MnO_2 and Co_3O_4/MnO_2 nanocomposites using a template-free, cost-effective, simple, and rapid co-precipitation technique [43].

2. Experimental section

2.1. Chemical and materials

All chemicals employed in this experiment were acquired from commercial dealers of analytical rank and were utilized as received without additional purification. Manganese sulfate monohydrate (99 %, $MnSO_4.H_2O$, India (Sisco Research Laboratories Pvt. Ltd.)), Cobalt (II) nitrate hexahydrate (99.5%, $Co(NO_3)_2.6H_2O$) and ammonia (China (Sinopharm Chemical Reagent Co., Ltd.)). Sodium hydroxide (NaOH, 99.5%)), Vulcan XC 72 carbon powder (96.5%), potassium hydroxide (97.5%, KOH), potassium permanganate (99.5%, $KMnO_4$), ethanol (98.5%), and sodium carbonate (97.5%) were obtained from Alpha Chemika (India). Throughout the experiments distilled water (DW) was employed as the solvent.

2.2. Synthesis of MnO_2 NPs

Nanoparticles (NPs) of MnO_2 were synthesized via a co-precipitation method. In a typical procedure, 5.07g of $MnSO_4.H_2O$ was dissolved in DW (100 mL) with vigorously stirring. Then, 3.16 g of $KMnO_4$ was dissolved in DW of 100 mL and mixed dropwise to the earlier suspension. The mixture was vigorously stirred at 80 °C for 5 h. While stirring, 0.2 M solution of NaOH was added to adjust the pH of the mixture to be 11. A precipitate of as-prepared MnO_2 was obtained. The precipitant was cleaned with DW and filtered. Finally, the obtained nanoparticles were dried at 100 °C for 6 h.

2.3. Synthesis of Co_3O_4 NPs

Co_3O_4 nanoparticles were prepared via co-precipitation method. In this typical experiment, 4.575 g (0.025M) of $Co(NO_3)_2$ was dissolved in 100 mL DW, and stirred for 20 min. After stirring, 20 mL sodium carbonate solution (1M) as precipitating agent becomes delivered to the above solution. Then, the mixtures were stirred for 6 h at 60 °C. After 6 h stirring, light purple coloration precipitates were filtered, washed with DW and absolute ethanol, respectively. Then, the final products obtained were dried inside an oven at 80 °C for 12 h. Finally, as prepared catalyst was calcined in an electric furnace for 3 h at 500 °C.

2.4. Synthesis of Co_3O_4/MnO_2 nanocomposites

Co_3O_4/MnO_2 nanocomposites were synthesized using a co-precipitation approach. In a typical synthesis, 0.5 g $Co(NO_3)_2.6H_2O$ was dissolved in 40 mL of DI water followed by mixing of 15 mL of 1.3 M aqua ammonia into the mixture under vigorous stirring condition. The color of the solution was changed to green at first, and was changed to dark green later. Then, 0.125 g of synthesized MnO_2 nanomaterials was dispersed in the above mixture and stirred for 1 h. The synthesized NPs were then filtered and washed with ethanol and DW followed by drying at 80 °C for 10 h to remove water and other organic substances. Lastly, the as-prepared NPs were calcined at 600 °C for 1 h in air. Mn/Co catalysts with various molar ratios (1:5, 1:4, 1:3, 1:2 and 1:1) of the Co_3O_4/MnO_2 catalysts were developed via a similar preparation method. Figure 1 shows detailed of the preparation process of Co_3O_4/MnO_2 nanocomposites via a co-precipitation method. From now onwards MnO_2 was used for pure MnO_2 and Co_3O_4/MnO_2-1-5, Co_3O_4/MnO_2-1-4, Co_3O_4/MnO_2-1-3, Co_3O_4/MnO_2-1-2, and Co_3O_4/MnO_2-1-1 were employed for Co_3O_4/MnO_2 nanocomposites with Co/Mn molar ratios of 1:5, 1:4, 1:3, 1:2 and 1:1 respectively.

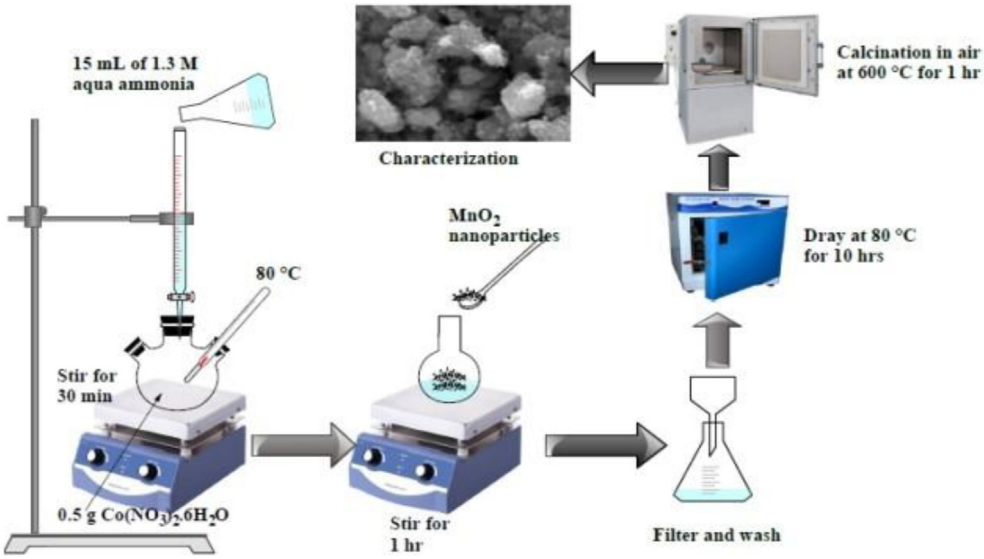

Figure 1. Diagram representation of development of Co_3O_4/MnO_2 nanocomposites via co-precipitation method.

2.5. Characterization

Scanning electron microscope (SEM, Inspect™ F50) was employed for morphology study. The XRD profile of developed NPs were examined using X-ray diffraction (XRD) with Cu-K_α radiation (MAXima_X XRD-7000, SHIMADZU) and were measured in 2-theta angle ranging from 10° and 80° at room temperature. FTIR (wavelength range of 400-4000cm^{-1}, FT-IR 6660, JASCO MODEL) was utilized to examine the functional groups. UV-Vis spectrometer (Lambda 35, PerkinElmer) was utilized to investigate the optical characteristics of the developed NPs. The thermal behavior analysis was accomplished via TGA/DTA technique. Quanta chrome Nova Win (version 11.0) was used to study the surface areas of as-synthesized NPs. The elemental examination was done through inductively coupled plasma optical emission spectrometry (ICP-OES, Perkin-Elmer 800).

2.6. Electrochemical measurement

For electrochemical measurements a 3-electrode half-cell comprising of glassy carbon electrode (GCE), Ag/AgCl and platinum coil were employed as the working, reference and counter electrodes, respectively. This procedure was used to examine the ORR performance of the MnO_2 and Co_3O_4/MnO_2 nanocomposites in a KOH (0.1 M) aqueous electrolyte. The working electrode has been developed by keeping MnO_2 and Co_3O_4/MnO_2 nanocomposite suspensions on a substrate (glassy carbon). The catalyst suspension was developed by mixing MnO_2 and Co_3O_4/MnO_2

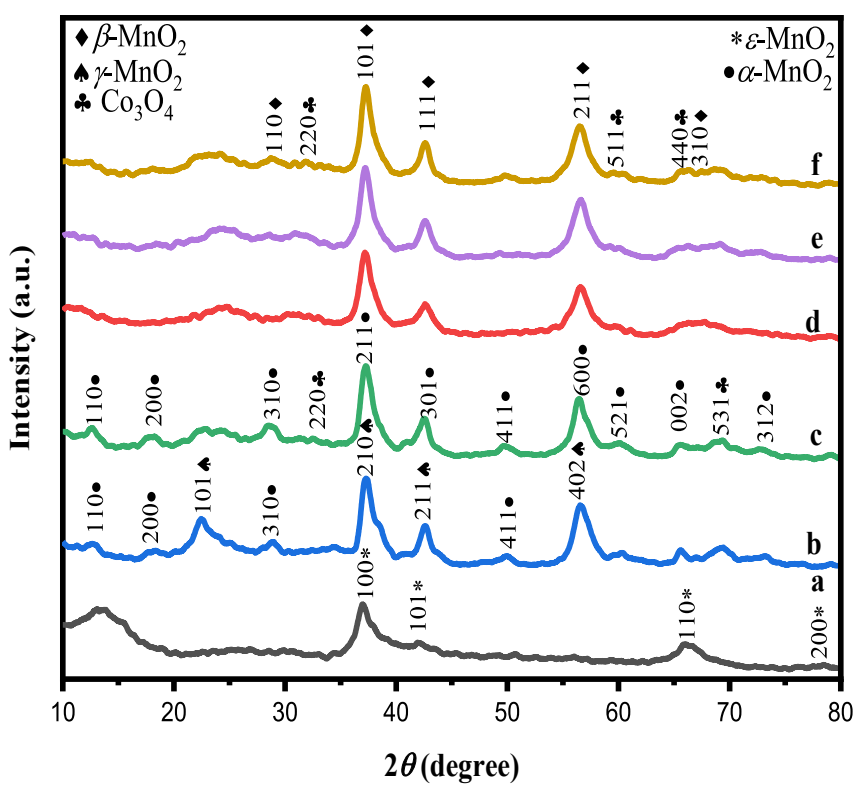

Figure 2. XRD profile of (a) MnO_2, (b) Co_3O_4/MnO_2-1-3, (c) Co_3O_4/MnO_2-1-4, (d) Co_3O_4/MnO_2-1-5, (e) Co_3O_4/MnO_2-1-2, (f) Co_3O_4/MnO_2-1-1 nanocomposites.

Table 1. Crystallite characteristics and micro-strain values calculated from XRD data of MnO_2 and Co_3O_4/MnO_2 nanocomposites.

Nanomaterials	$\delta \times 10^3$ (nm^{-2})	Crystal systems	Intercept	Crystallite size (nm)		Strain(ε) (W–H plot)
				Sherrer	W–H	
MnO_2	199.29	Hexagonal	-0.0969	2.24	1.43	0.17038
Co_3O_4/MnO_2 -1-5	28.82	Tetragonal & Cubic	-0.02459	5.89	5.63	-5.05873
Co_3O_4/MnO_2 -1-4	34.29	Tetragonal &Cubic	-0.07731	5.4	1.79	-0.02941
Co_3O_4/MnO_2 -1-3	43.40	Complex tunnel, Tetragonal & Cubic	0.04706	4.8	2.94	0.01613
Co_3O_4/MnO_2 -1-2	59.49	Tetragonal & Cubic	-0.12931	4.1	1.07	-0.03866
Co_3O_4/MnO_2 -1-1	81.63	Tetragonal & Cubic	0.18565	3.5	0.75	-0.08259

nanocomposites (5.0 mg) with carbon powder (5.0 mg) to maintain an electronic conductivity in 2.5 ml isopropanol-water solution with 7:3 volume/volume ratios. The catalyst ink was ultrasonically mixed for 10 min and then 8 μL of the prepared suspension was pipetted onto the GCE electrode. Before each measurement (electrochemical), the electrolyte (KOH, 0.1 M) was saturated by purging high purity oxygen/nitrogen for a minimum of 30 min. The oxygen/nitrogen atmosphere was kept in the electrocatalytic measurements. CHI760E electrochemical workstation was utilized for LSV (5 mV s^{-1}) and CV (5, 10, 20, 50, and 100 mV s^{-1}) measurements in the potential window interval of +0.1 to -0.7 V (vs Ag/AgCl).

3. Results and discussion

3.1. Structural characterization

XRD was conducted to study the crystal structure and composition of the developed nanoparticles over the 2 theta ranges of 10°–80° with a scan rate of 0.02°/s. The XRD profile of pure MnO_2 and Co_3O_4/MnO_2 nanocomposites at molar ratios of (1:5, 1:4, 1:3, 1:2 and 1:1) are shown in Figure 2. In the XRD patterns of MnO_2 NPs, the diffraction peaks observed at 37.22°, 42.05°, 66.14°, and 78.45° matched well to the (1 0 0), (1 0 1), (1 1 0), and (2 0 0) lattice plane, which are assigned to ε-Mn O $_2$ (JCPDS 00-030-0820) diffraction pattern. In the XRD pattern of the Co_3O_4/MnO_2-1-3 hybrid material, the diffraction peaks at 22.38°, 37.42°, 42.69° and 56.57° correspond to the (101), (210), (211), and (402) crystal planes of γ-MnO_2 (JCPDS No: 14–0644), respectively. The diffraction peaks at 12.60°, 17.95°, 28.90°, and 37.42° (coinciding with γ-MnO_2), 49.94°, 65.62°, and 69.51° were assigned to α-Mn O $_2$ (JCPDS 44–0141), whereas the diffraction peaks at 32.69° and 69.06° assigned to the (220) and (531) crystal planes of Co_3O_4 (JCPDS No: 00-042-1467), respectively [44]. Hence, these indicate that the sample consists of three phases (γ-Mn O $_2$, α-Mn O $_2$ and Co_3O_4). Similarly, the XRD pattern of the Co_3O_4/MnO_2-1-4 nanocomposites showed diffraction peaks at 12.60°, 18.12°, 28.48°, 37.10°, 42.47°, 49.83°, 56.47°, 60.15°, 65.62°, and 72.56° which were assigned to (110), (200), (310), (211), (301), (411), (600), (521), (002), and (312) crystal planes of α-Mn O $_2$ (JCPDS No: 44–0141), correspondingly; and the diffraction peaks at 32.69° and 69.06° were assigned to the (220) and (531) crystal planes of Co_3O_4 (JCPDS No: 00-042-1467), respectively [44]. The above results confirm the development of the Co_3O_4/MnO_2 nanocomposites. In the XRD profile of Co_3O_4/MnO_2-1-5, Co_3O_4/MnO_2-1-2, and Co_3O_4/MnO_2-1-1 nanocomposites, the diffraction peaks at 28.69°, 37.32°, 42.47°, 56.64°, 59.47°, and 67.41° were matched well to the (110), (101), (111), (211), (220), and (310) lattice plane of β-Mn O $_2$ (JCPDS No: 00-024-0735), respectively [45] and the diffraction peaks at 31.95°, 59.51°, and 65.62° corresponding to the (220), (511), and (440) lattice plane of Co_3O_4 (JCPDS No: 00-043-1003), respectively [46]. Therefore, the samples were included of two phases Co_3O_4 and MnO_2. Therefore, the above results display that the phase of ε-Mn O $_2$ was transformed into a different structure after the addition of Co_3O_4. As shown in Table 1, the addition of Co_3O_4 affected the basic structure of the ε-Mn O $_2$ nanoparticles.

3.2. Crystallite size and strain study

3.2.1. Debye-Scherrer technique

Debye-Scherrer method (equation 1) was used to estimate the average crystallite sizes of pure MnO_2 and Co_3O_4/MnO_2 nanocomposites at different molar ratios [36, 47].

$$D = \frac{K\lambda}{\beta\cos\theta} \tag{1}$$

where, K, D, β, λ and θ are the Scherer constant, the crystallite size, full width at the half maximum intensity, the x-ray sources wavelength and peak position, correspondingly [48]. The average value of the crystallite size of pure MnO_2, Co_3O_4/MnO_2-1-5, Co_3O_4/MnO_2-1-4, Co_3O_4/MnO_2-1-3, Co_3O_4/MnO_2-1-2, Co_3O_4/MnO_2-1-1 nanocomposites were 2.24, 5.89, 5.4, 4.8, 4.1, and 3.5 nm, correspondingly as displayed in Table 1 [49]. Moreover, the dislocation density (δ) and strain (ε) of the electrocatalyst are additional critical factors which may be determined using the XRD data (Table 1). The δ values for all catalysts were determined by employing equation (2).

$$\delta = 1/D^2 \tag{2}$$

where δ and D were dislocation density and crystallite size, respectively. The result shows that δ values increased after the addition of the dopant (Table 1).

3.2.2. Williamson-Hall technique

The crystallite size *(D)* and the microstrain (ε) of prepared NPs were computed via Williamson-Hall plot using Eq. (3) [6]:

$$\beta\cos\theta = \frac{K\lambda}{D} + 4\varepsilon\sin\theta \tag{3}$$

where, λ, ε, D, β and K are the wavelength, microstrain, crystallite size, full width hall maximum, and shape factor, correspondingly. A straight line was found by plotting $\beta\cos\theta$ (y-axis) versus $4\sin\theta$ (x-axis) and the value of the crystallite size was determined from the intercept while the value of the microstrain was determined from the slope (Figure 3) [50]. Crystallite size of 1.43 nm, 5.6 nm, 1.79 nm, 2.94 nm, 1.07 nm, and 0.75 nm were obtained for MnO_2, Co_3O_4/MnO_2-1-5, Co_3O_4/MnO_2-1-4, Co_3O_4/MnO_2-1-3, Co_3O_4/MnO_2-1-2, and Co_3O_4/MnO_2-1-1, respectively as presented in Table 1. The results show that both methods have similar crystallite sizes while showing a slight size difference. This could be because of the appearance of various particle geometries. Moreover, a -ve slope in the plot illustrates the behavior of compressive strain, whereas, the appearance of a +ve slope indicates tensile strain, which is agreed with our results [51].

3.3. ICP-OES analysis

The elemental analysis was investigated via ICP-OES to verify the amount of Co and Mn in the nanocomposites. ICP-OES samples were prepared by dissolving the as-synthesized materials in acidic solution of HNO_3:HCl, 1:3 v/v by volume. Hence, the ICP-OES analysis of the

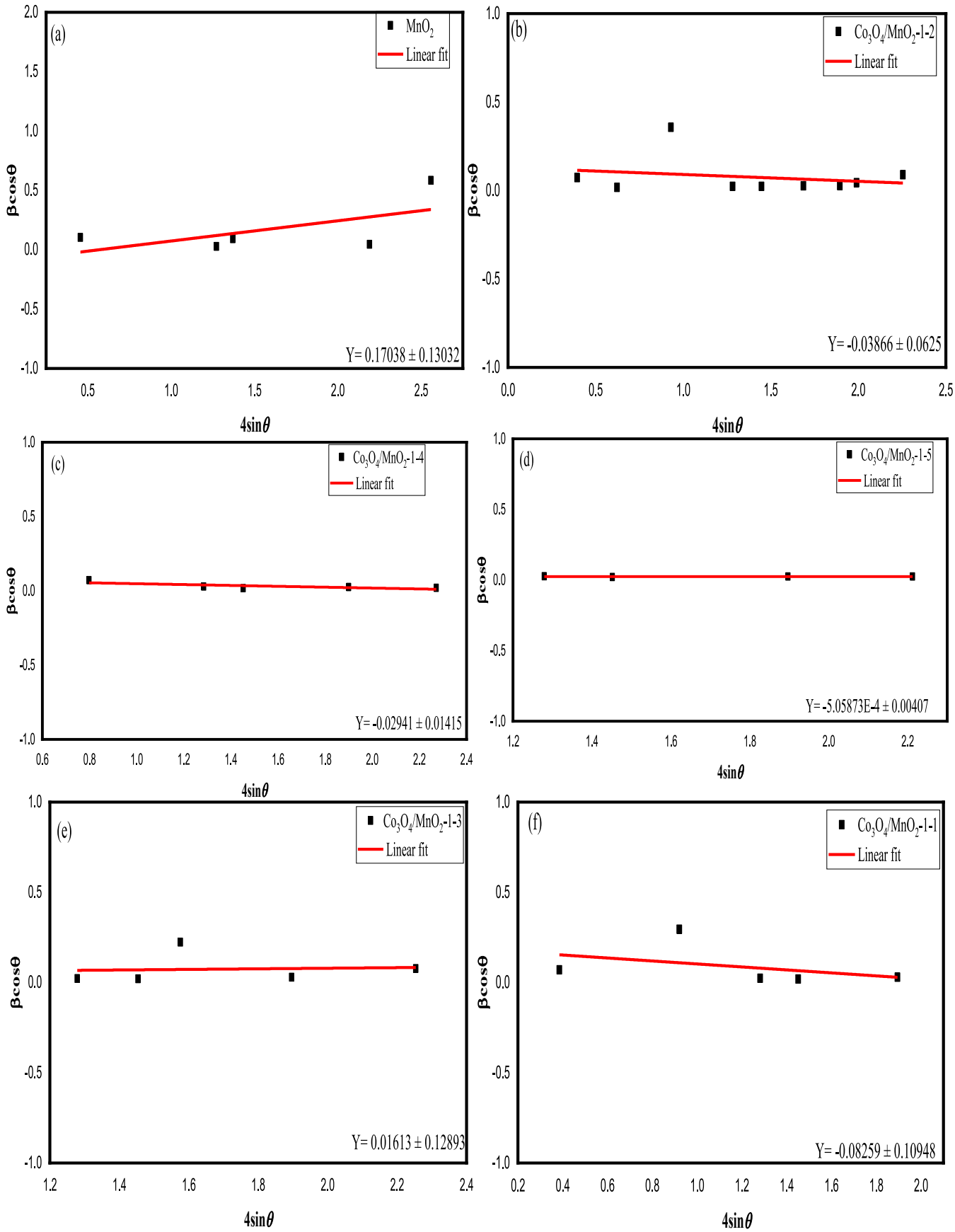

Figure 3. Williamson Hall scheme of (a) MnO_2, (b) Co_3O_4/MnO_2-1-2, (c) Co_3O_4/MnO_2-1-4, (d) Co_3O_4/MnO_2-1-5, (e) Co_3O_4/MnO_2-1-3 and (f) Co_3O_4/MnO_2-1-1 nanocomposites.

Table 2. Co_3O_4/MnO_2 nanocomposites analysis results via ICP-OES. (All values are in (mmol/L) except Co/Mn).

Nanomaterials	Co	Mn	Co/Mn
Co_3O_4/MnO_2-1-5	0.37	1.955	0.18
Co_3O_4/MnO_2-1-4	0.39	1.713	0.23
Co_3O_4/MnO_2-1-3	0.45	1.524	0.29
Co_3O_4/MnO_2-1-2	0.72	1.436	0.5
Co_3O_4/MnO_2-1-1	0.854	1.325	0.64

amount of Co and Mn in the nanocomposites showed that Co_3O_4/MnO_2-1-1sample has the higher Co and Mn content than the others, which will affect electrochemical, thermal, and structural characteristics of the nanomaterials [52]. Table 2 presents the amount of Co and Mn in the nanocomposites samples. The results showed that, the Co/Mn molar ratio in Co_3O_4/MnO_2-1-5, Co_3O_4/MnO_2-1-4, Co_3O_4/MnO_2-1-3, Co_3O_4/MnO_2-1-2 and Co_3O_4/MnO_2-1-1 samples were 0.18, 0.23, 0.29, 0.5 and 0.64, respectively, in the composite materials. The results reveal that as the amount of MnO_2 increases the molar ratio of Co/Mn decreases accordingly.

3.4. BET surface area study

The surface areas of MnO_2 NPs and Co_3O_4/MnO_2 nanocomposites have been examined using the BET analysis technique. Table 3 displays the BET surface area, pore volume and pore radius of as-prepared nanomaterials. The BET surface areas for the Co_3O_4, MnO_2, and Co_3O_4/MnO_2-1-1 are 80.217, 106.75 and 193.386 $m^2\ g^{-1}$, respectively. This shows that a higher surface area is conducive to the shuttle and storage of ions and electrons in the electrode, providing more active sites, thereby improving electrochemical performance [53]. Moreover, the corresponding pore sizes were determined to be 3.338, 3.471, 7 and 3.357 nm for Co_3O_4, MnO_2, and Co_3O_4/MnO_2-1-1 nanocomposites, respectively. The porous structure promotes the diffusion and transfer of ions in the electrolyte during the charging/discharging process. Thus, the combination of MnO_2 and Co_3O_4 sample leads to increasing of the surface area and reduction of the average pore size [54].

3.5. Morphological characterization

The surface morphologies of the MnO_2 and Co_3O_4/MnO_2 nanocomposites were investigated by SEM (Figures 4, 5, and 6). SEM images of pure MnO_2 prepared by the co-prescription method exhibited high mono dispersed flower-like nanostructures (Figure 4) [55, 56]. SEM image of the Co_3O_4/MnO_2-1-5 nanocomposite is shown in Figure 5. The addition of Co_3O_4 at different ratios influenced the morphology of the MnO_2 nanoparticles. Thus, the Co_3O_4/MnO_2 nanocomposites at a 1:5 M ratio exhibited aggregated nanoparticles with a porous surface. However, with a 1:1molar ratio of Co_3O_4 and MnO_2 a homogenous small needle-like appearance was obtained as presented in Figure 6 [50, 57]. Moreover, SEM illustrations shows that the development of MnO_2, Co_3O_4/MnO_2-1-5, and Co_3O_4/MnO_2-1-1 with an average particle diameter of 8.23 nm, 14.43 nm, and 7.85 nm, respectively. ImageJ software (version 1.8.0_112) was used to examine the diameter of as-synthesized nanomaterials of the SEM images via a histogram plot of particle size distribution (Figure 7(a-c)) in order to generate the histogram plot displaying particle size distribution for approximately 500 nm particles have been counted. The results show that Co_3O_4/MnO_2-1-1 has the lowest diameter and regular morphology, whereas Co_3O_4/MnO_2-1-5 has the highest diameter geometry. Therefore, the Co/Mn molar ratio plays a significant role in the fabrication of nanocomposite morphology.

Table 3. Surface area investigation of Co_3O_4, MnO_2 and Co_3O_4/MnO_2 nanocomposites.

Nanoparticles	BET surface area (m^2/g)	Total pore volume (cc/g)	Average pore size (nm)
Co_3O_4	80.217	0.250	3.338
MnO_2	106.75	0.319	3.471
Co_3O_4/MnO_2-1-1	193.386	0.604	3.357

3.6. FTIR analysis

FTIR spectroscopic studies of both pure MnO_2 and Co_3O_4/MnO_2 nanocomposites at various Co/Mn molar ratios were performed to identify the functional groups. The stretching and bending characteristics of various groups were analyzed in the 400 - 4000 cm^{-1} wavelength ranges (Figure 8). As displayed in Figure 8, the band around 3411 cm^{-1} shows the O–H stretching of H_2O and the weak band at approximately at 1633 cm^{-1} might be because of the bending vibration of O–H groups in the molecules of adsorbed water [49]. The peaks at around 1388 cm^{-1} and 1095 cm^{-1} are associated to O–H. However, the distinctive peaks at 592 cm^{-1} and 520 cm^{-1} can be matched to the stretching vibrations of M-O (M = Co, Mn). Moreover, the presence of M-O and O–H spectra was observed from the FTIR pattern of pure MnO_2 and Co_3O_4/MnO_2 [58].

Figure 9 displays the FTIR spectra of un-calcined and calcined Co_3O_4 nanomaterials. The FTIR spectrum of Co_3O_4 nanoparticles shows that the broad bands around 3440 cm^{-1} is corresponding to stretching vibration of the O–H group of molecular water and the band at 1632 cm^{-1} is matched to the bending mode of water molecules [59]. The bands at 1387 and 1074 cm^{-1} are ascribed to the vibration of the surface bidentate carbonate from gaseous CO_2 which interacts with the lattice oxygen present in Co_3O_4 [60]. However, after annealing treatment, for the as-prepared nanoparticles a very strong peak at 655 cm^{-1} for characteristic of spinel Co_3O_4 is noticed which is consistent to those recently reported values in the literature. The peaks around 655 and 520 cm^{-1} are associated to vibration of the Co–O bond in Co_3O_4 [61].

3.7. Optical property analysis

The UV-Visible absorbance spectra of pure MnO_2 and Co_3O_4/MnO_2 nanocomposites were studied in 200–800 nm wavelength range of the electromagnetic spectrum (Figure 10). The absorption peaks for pure MnO_2 were observed at 280 nm in the UV region while the absorption bands for Co_3O_4/MnO_2-1-5, and Co_3O_4/MnO_2-1-1 were observed at 379 and 382 nm, respectively (Figure 10(a)). The band gaps values of the MnO_2 and Co_3O_4/MnO_2 nanocomposites were estimated using the Tauc relationship (equation 4).

$$(\alpha h\nu)^n = A(h\nu - E_g) \tag{4}$$

where, $h\nu$ α, A, Eg, $n = ½$, and $n = 2$ are the energy of photons, the absorption coefficient, a constant, the energy band gap, the indirect transition and the direct transition, respectively. The computed optical band gap for MnO_2, Co_3O_4/MnO_2-1-5, and Co_3O_4/MnO_2-1-1 nanocomposites were 3.07 eV 2.6 eV, and 2.3 eV, correspondingly. Moreover, the band gap energy values of the as-prepared catalysts were assessed via extrapolating linear section of the sketches $(\alpha h\nu)^2$ with respect to $(h\nu)$ as revealed in Figure 10 (b).

3.8. TGA/DTA study

The thermal characteristics of the Co_3O_4, MnO_2 and Co_3O_4/MnO_2 nanocomposite catalysts were studied using TGA and DTA. The analysis was performed by taking 8 mg of the synthesized materials in the range of 30–900 °C at a rate of 15 °C/min in an air atmosphere. Figure 11 displays the TGA/DTA curves of Co_3O_4, MnO_2 and Co_3O_4/MnO_2 nanocomposites. The TGA profile of the pure MnO_2 NPs illustrates three steps of weight loss. In the first step 0.25 mg weight was lost before 129 °C, which can be associated with the loss of surface bonded water. In the second step 0.58

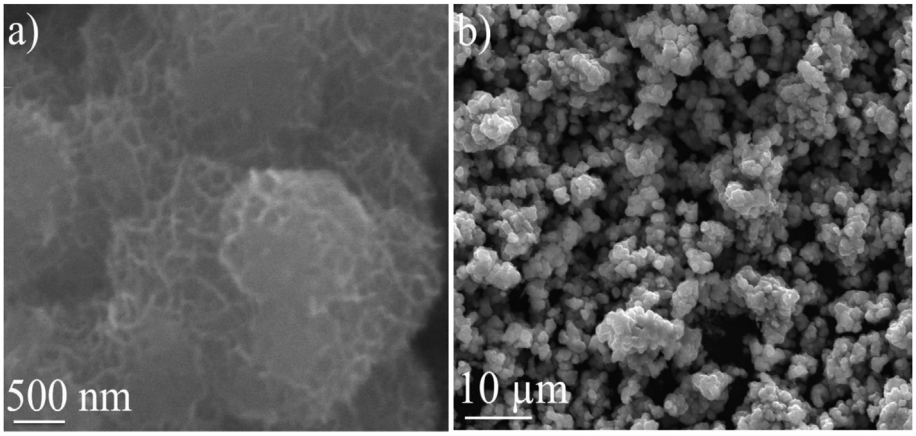

Figure 4. SEM image of (a) MnO_2 NPs at 500 nm and (b) MnO_2 NPs at 10 μm.

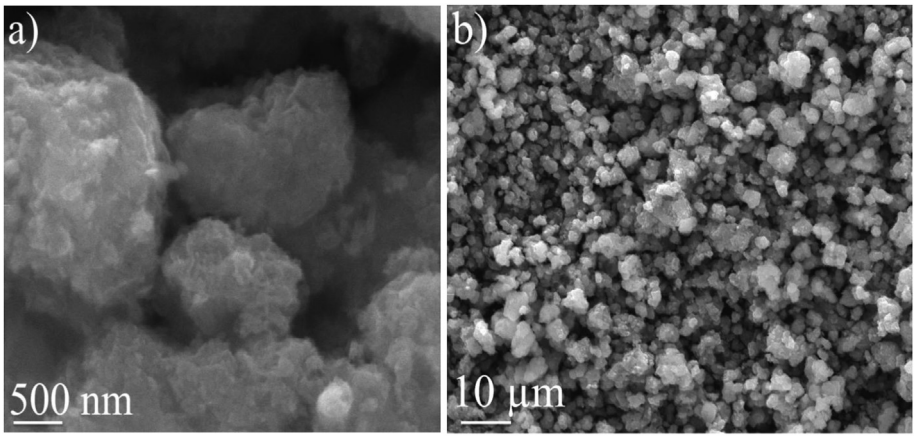

Figure 5. SEM images of (a) Co_3O_4/MnO_2-1-5 at 500 nm, (b) Co_3O_4/MnO_2-1-5 at 10μm.

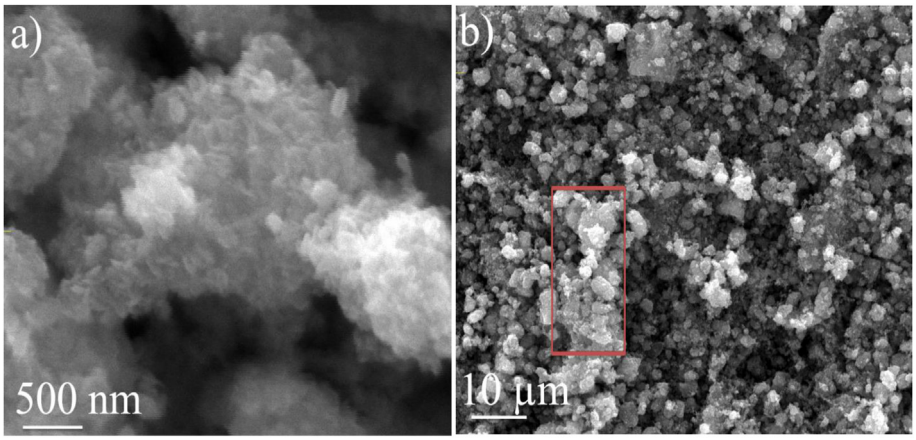

Figure 6. SEM images of (a) Co_3O_4/MnO_2-1-1 at 500 nm and (b) Co_3O_4/MnO_2-1-1 at 10μm.

mg of weight was lost in the range of 129–556 °C, which can be attributed to the loss of lattice oxygen and phase transformation of MnO_2 to Mn_2O_3. And the third step weight loss of 0.29 mg, which may lead to additional lattice oxygen and phase transformation of Mn_2O_3 to Mn_3O_4 [62]. Similarly, the TGA profiles of the Co_3O_4/MnO_2-1-1 nanocomposites showed three steps of weight losses. The primary weight loss of 0.3 mg appeared before 164 °C showing the loss of surface adsorbed water. In the second step, the sample (0.54 mg) was lost in the range of 164–563 °C a phase transformation of MnO_2 to Mn_2O_3 and the reduction of Co_3O_4 to CoO. The third step of weight loss (0.16 mg) occurred at 563–795 °C leading to additional lattice oxygen and reduction of Mn_2O_3 to Mn_3O_4. As shown in Figure 11 the analysis was started with 8 mg of sample and then 6.88 mg and 7 mg of MnO_2 and Co_3O_4/MnO_2, respectively were obtained after heating to 900 °C, resulting in weight loss of 14% and 12.5 % of MnO_2 and Co_3O_4/MnO_2, respectively. The DTA curve for MnO_2 displays endothermic peak around 67.4 °C, which could be due to the evaporation of surface adsorbed water molecules while the large peaks at 532.7 and 609.3 °C represent the phase conversion of MnO_2 to Mn_2O_3 and from

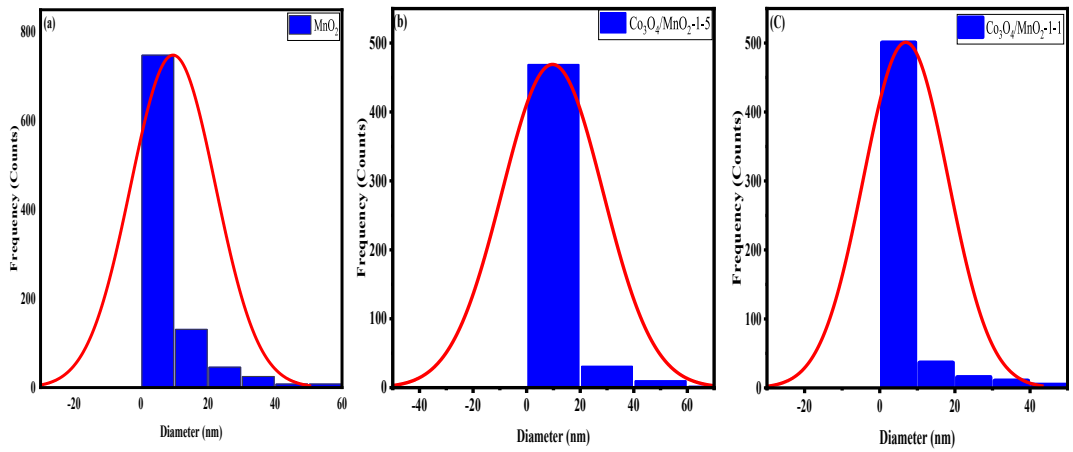

Figure 7. A histogram sketch of particle size distribution of nanomaterials extracted from SEM images of (a) MnO_2, (b) Co_3O_4/MnO_2-1-5, and (c) Co_3O_4/MnO_2-1-1.

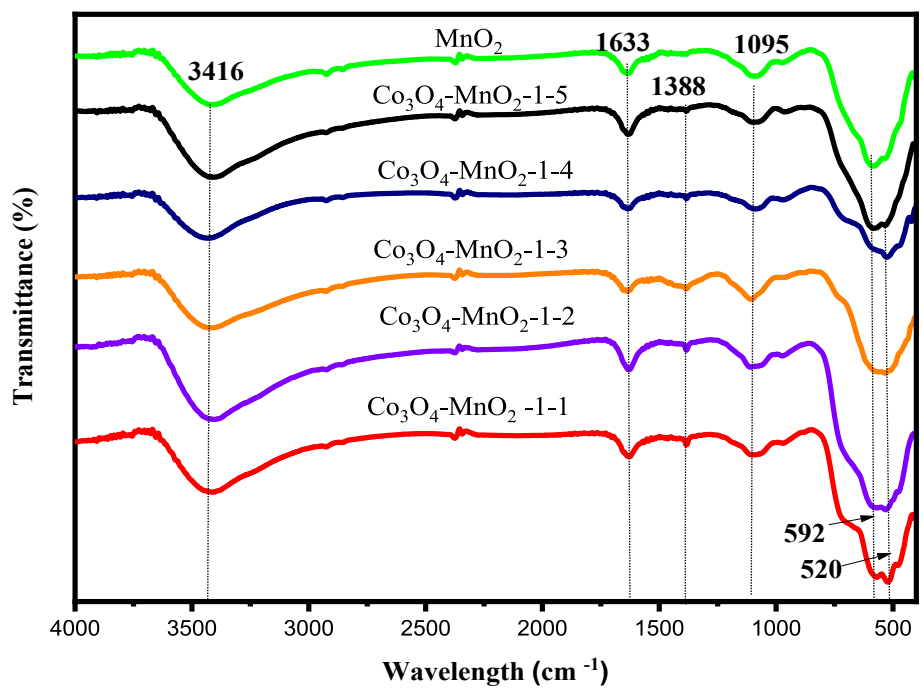

Figure 8. FTIR spectra of Co_3O_4/MnO_2-1-1, Co_3O_4/MnO_2-1-2, Co_3O_4/MnO_2-1-3, Co_3O_4/MnO_2-1-4, Co_3O_4/MnO_2-1-5, and MnO_2 nanocomposites.

Mn_2O_3 to Mn_3O_4, correspondingly (Figure 11 (a)). Similarly, the DTA profile of the Co_3O_4/MnO_2 nanocomposite is shown in Figure 11 (b). As exhibited in Figure 11 (b) peak around 84.8 °C was observed and this might be because of the evaporation of the bonded molecules of water. Moreover, the sharp peak was appeared at 533.5 °C and this could be owing to the phase conversion of MnO_2 to Mn_2O_3 while the peak at 589 °C might be because of a phase transformation from Mn_2O_3 to Mn_3O_4 and a reduction of Co_3O_4 to CoO [63]. Figure 11 (c) shows the thermal characteristics of Co_3O_4 nanoparticles, which proceed in three stage mass decomposition. In the first step 0.3 mg of sample was lost before 230 °C, which shows the loss of surface adsorbed water [64]. The second (0.78 mg) and third (0.4 mg) mass lost in the range of 230–437 °C and 437–698 °C were related to the decomposition of the remaining organic ligands with corresponding DTA curve at 393.2, 407.88, and 545.39 °C. However, no change is observed after 698 °C of the TGA/DTA thermal analysis patterns of Co_3O_4 nanoparticles. Thus, Co_3O_4 nanoparticles showed total weight loss of 17.5 %. Hence, the Co_3O_4, MnO_2 and Co_3O_4/MnO_2 catalysts exhibited quite different thermal characteristics because of the synergetic outcome of $Co_3O_4$and MnO_2 nanomaterials. Co_3O_4/MnO_2 displayed a much stronger thermal stability with weight loss of 12.5 %.

3.9. Electrochemical characterization

3.9.1. CV study

The electrochemical ORR activities of the as-synthesized Co_3O_4, MnO_2 and Co_3O_4/MnO_2 nanocomposites modified electrodes were studied via CV under O_2 saturated atmosphere in KOH (0.1 M) aqueous medium (Figure 12) However, Figure 12 curve (c) shows the CV curve of Co_3O_4/MnO_2-1-1 modified electrode under N_2 saturated atmosphere. The oxygen reduction peaks for the as-synthesized Co_3O_4, MnO_2, Co_3O_4/MnO_2-1-1, Co_3O_4/MnO_2-1-2 and Co_3O_4/MnO_2-1-5 saturated

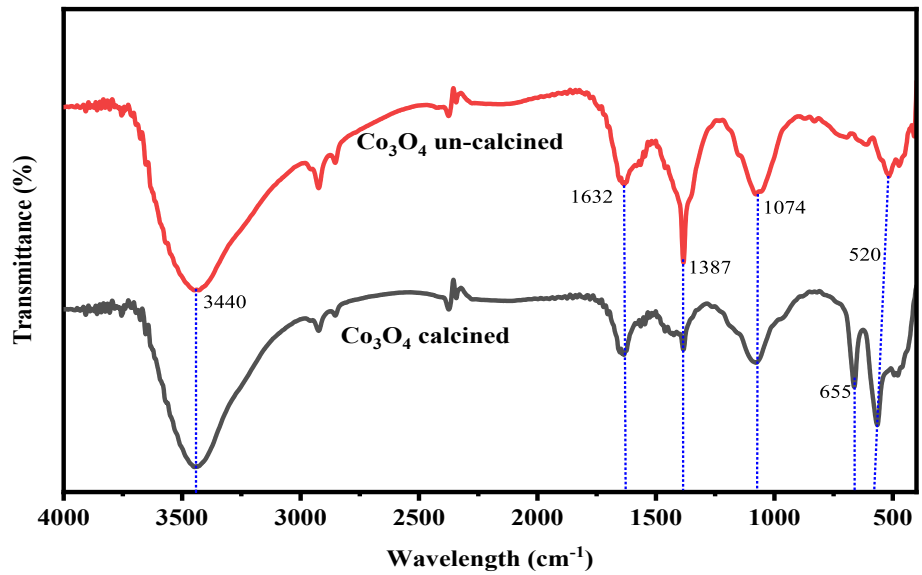

Figure 9. FTIR spectra of un-calcined and calcined Co_3O_4 nanomaterials.

nanocomposite materials were found at -0.444 V, -0.468 V, -0.352 V, -0.352 V and -0.36 V (vs Ag/AgCl), respectively as displayed in Figure 12. Moreover, a sharp reduction peak was not observed in the oxygen reduction peak for the as-synthesized Co_3O_4/MnO_2-1-1 in N_2 saturated atmosphere which is reliable with earlier reported results [65]. The transformation of the ORR peak toward a positive potential can be associated with a reduction in the overpotential, which enhances the ORR activity of the corresponding catalyst [66, 67]. Therefore, the reduction peak potential of the Co_3O_4/MnO_2-1-1 electrode was shifted by 116 mV to the positive side as compared with that of the MnO_2 electrode. The current intensity of Co_3O_4/MnO_2-1-1modified electrode is greater that of other electrodes. The influence of saturation in oxygen in the process of catalysis was also assessed. As shown in Figure 12, the red line is the CV pattern of Co_3O_4/MnO_2-1-1in the presence of oxygen and the blue line belong to the CV pattern of Co_3O_4/MnO_2-1-1in the absence of oxygen. The result showed that oxygen in the cell increases the activity of the catalysts for ORR. The CV plot of MnO_2 and Co_3O_4/MnO_2-1-1 nanocomposites at different scan rates are provided in Figure 13 (a, b). It is perceived from the CV plot that the reduction peaks are shifted to a low potential values with an increasing in sweeping rates. At the low scan rate, both MnO_2 and Co_3O_4/MnO_2-1-1 nanocomposite material show good catalytic activity, which shows irreversible electrode. Generally, Co_3O_4/MnO_2-1-1 nanocomposite shows improved catalytic performance to ORR as well as improved electrical conductivity. This may be because of the synergistic impacts of MnO_2 and Co_3O_4. Based on the above investigation, the catalytic behaviors of Co_3O_4/MnO_2-1-1 nanocomposite can be ascribed to the synergy between manganese dioxide and cobalt oxide nanoparticles, which increases the surface area of Co_3O_4/MnO_2 nanocomposite as confirmed via BET examination. The ORR catalytic activity mechanism of Co_3O_4 and MnO_2 is described in Eqs. (5), (6), (7), (8), (9), (10), (11), (12), (13), (14), and (15). The two classic oxygen catalysts are metal oxides and metals, and the ORR mechanism by these catalysts has been intensively investigated. For metal-based catalysts (e.g. platinum), based on the kind of oxygen adsorption, a four-electron approach or a two-electron approach can be used for ORR. The two kinds of adsorption are terminal and bidentate O_2 adsorption which correspond to a two-electron and a direct four-electron pathway, respectively. The bidentate adsorptions are given as in Eqs. (5), (6), and (7) and the end-on adsorption reactions are written as in Eqs. (8), (9), and (10) [68]:

$$O_2 + H_2O + 2e^- \rightarrow 2HO_{ads} + 2OH^- \quad (5)$$

$$2HO_{ads} + 2e^- \rightarrow 2OH^- \quad (6)$$

$$\text{Overall: } O_2 + H_2O + 4e^- \rightarrow 4OH^- \quad (7)$$

$$H_2O + O_2 + 2e^- \rightarrow HO_{2,ads} + 2OH^- \quad (8)$$

$$HO_{2,ads} + e^- \rightarrow HO_2^- \quad (9)$$

$$\text{Overall: } O_2 + H_2O + 2e^- \rightarrow HO_2^- + 4OH^- \quad (10)$$

These two-electron reactions can be followed by further $2e^-$ peroxide reduction or chemical peroxide disproportionation as shown below (Eqs. (11) and (12)):

$$HO_2^- + H_2O + 2e^- \rightarrow 3OH^- \text{ (reduction of peroxide)} \quad (11)$$

Or

$$2HO_2^- \rightarrow 2OH^- + O_2 \text{ (disproportionation of peroxide)} \quad (12)$$

Moreover, metal oxide catalysts (i.e., Co_3O_4) follow the same ORR reaction principle on the surface with different charge distributions. However, oxygen atoms are not fully coordinated with surface cations of the stoichiometric oxide. In an aqueous electrolyte, the coordination of anions is completed through the oxygen of water molecules. Therefore, surface cations reduction via electrons from an external circuit is charge-compensated through surface oxygen ligands protonation. The reaction pathway of ORR on the surface of metal oxide is shown below (Eqs. (13), (14), and (15)) [69, 70]:

$$M^{m+} - O^{2-} + 2e^- + 2H_2O \rightarrow 2M^{(m-1)} + \text{-}OH^- + 2OH^- \quad (13)$$

$$O_2 + e^- \rightarrow O_{2,ads}^- \quad (14)$$

$$2M^{(m-1)+} \text{-} OH^- + O_{2,ads}^- + e^- \rightarrow 2M^{m+} - O^{2-} + 2OH^- \quad (15)$$

3.9.2. LSV analysis

Further to evaluate the electrochemical properties of the as-synthesized nanoparticles, LSV tests have been performed on Co_3O_4, MnO_2 and Co_3O_4/MnO_2 nanocomposites in an oxygen-saturated KOH (0.1 M) solution at 5 mV/s scan rate (Figure 14). The Co_3O_4, MnO_2 and Co_3O_4/MnO_2 nanocomposites peaks reduced at -0.381V and -0.366V and -0.363V (vs Ag/AgCl), correspondingly [71]. That the cathodic peak current of Co_3O_4/MnO_2-1-1 nanocomposites modified electrode is much greater than that of Co_3O_4 and MnO_2 modified electrodes confirming that Co_3O_4/MnO_2-1-1 nanocomposite has improved electrocatalytic activity

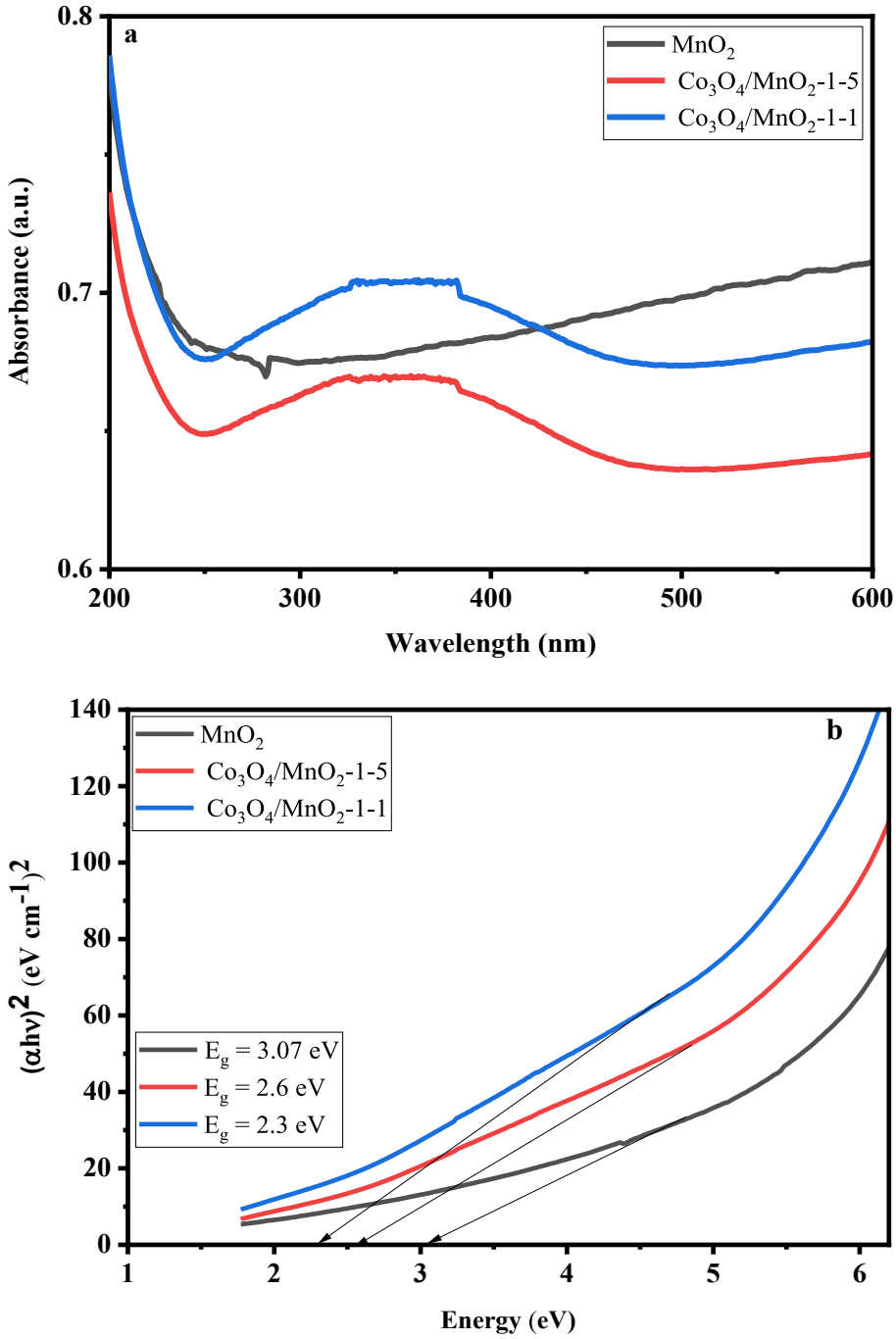

Figure 10. UV-Vis profile of (a) pure MnO_2, Co_3O_4/MnO_2-1-5, and Co_3O_4/MnO_2-1-1, nanocomposites and Tauc plot of (b) MnO_2, Co_3O_4/MnO_2-1-5, and Co_3O_4/MnO_2-1-1, nanocomposites.

for oxygen reduction. The analyses display that Co_3O_4/MnO_2-1-1 nanocomposites have higher current and higher peak potential then Co_3O_4 and MnO_2 electrocatalyst.

3.9.3. Scan rate effect

CV profile of Co_3O_4/MnO_2 nanocomposites tests were conducted at various scan rates (5–100 mV/s) using 0.1 M KOH aqueous electrolyte saturated with oxygen by a GCE (Figure 15). Therefore, Figure 15(a) shows the voltammetric analysis of Co_3O_4/MnO_2-1-1 NPs at various scan rate. Scan rate studies were made to confirm the ORR performance exhibited through the Co_3O_4/MnO_2-1-1 NPs due to diffusion, adsorption, or a combination of them. The result shows that the cathodic peak potential at -0.297 V (5 mV/s) moved to the -ve potential as the scan rate extended to -0.365 V (100 mV/s). Furthermore, the impact of the square root of the scan rate with respect to peak current is analyzed, and a linear relationship is observed in the range of 5–100 mV/s, as presented in Figure 15(b). The result is shown as the diffusion control process, and the regression analysis is expressed in Eq. (16) [72]:

$$I_{pc}\ (\mu A) = 0.2292\ v^{1/2}\ (V^{1/2}s^{-1/2})\ -\ 1.6343,\ (R^2 = 0.9775) \quad (16)$$

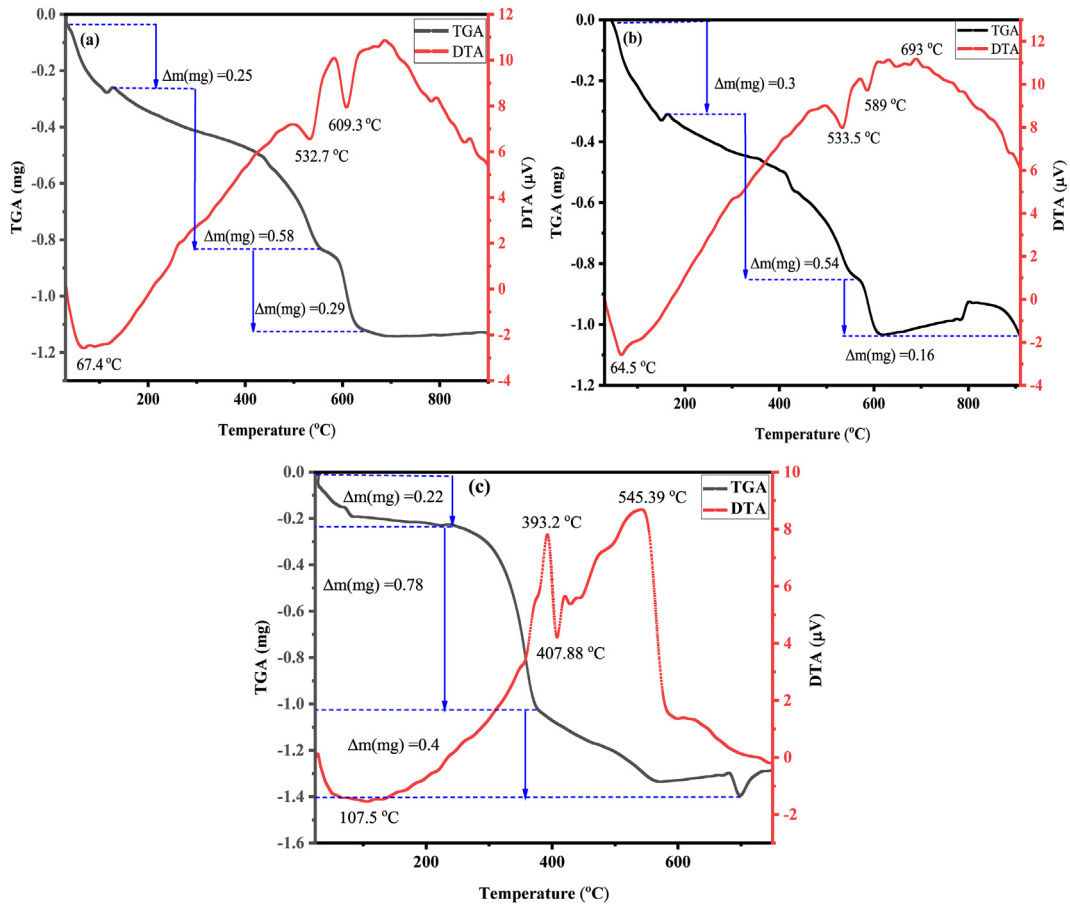

Figure 11. TGA/DTA graphs of (a) MnO_2 NPs, (b) Co_3O_4/MnO_2 nanocomposites and (c) Co_3O_4 NPs.

Figure 15(c) presents the cathodic peak current (i_{pc}) versus the scan rate (v). The presence of adsorbed electroactive species was confirmed via the linear relationship of v with peak current. Hence, ORR in the Co_3O_4/MnO_2/GCE electrode shows kinetic control and diffusion reactions, which involves in the adsorption of O_2 on the electrode surface. Moreover, the relation between logarithmic sweep rate with respect to peak potential was investigated (Figure 15(d)). The regression analysis of logarithm of the reduction potential with respect to the scan rate (5–100 mV/s) is presented in Eq. (17).

$$E_{pc}\ (V) = 0.331 \log v\ (Vs^{-1}) + 18.37,\ (R^2 = 0.9165) \tag{17}$$

Hence, the irreversible CV profile can be used to determine the transferred number of electrons into the reaction via Laviron method (equation 18) [73, 74]:

$$E_p = E^{0'} + \left(\frac{2.303\,RT}{\alpha nF}\right)\log\left(\frac{RT\,k^0}{\alpha nF}\right)\left(\frac{2.303\,RT}{\alpha nF}\right)\log v \tag{18}$$

where, $E^{0\prime}$, n, R, k^0, v, F, T and α are formal redox potential, transferred number of electrons, gas constant, standard heterogeneous rate constant of the reaction, scan rate (V s^{-1}), Faraday constant, temperature (K), and coefficient of transfer, correspondingly. Here, the αn value of 1.152 was obtained from calculated value of the slope of E_{pc} vs. log v (calculated value = 0.05135), F = 96480 C/mol, R = 8.314 J/K mol and T = 298 K. According to Bard and Faulkner, α can be computed by employing Eq. (19) [75, 76];

$$\alpha = \frac{47.7}{E_P - E_{\frac{p}{2}}}\ \text{mV} \tag{19}$$

where $E_{p/2}$ represents the potential at half of the peak value of the current. In addition, the estimated value of n to the electro-reduction process of O_2 on the Co_3O_4/MnO_2/GCE surface is 3.7. Hence, these results exhibited that the Co_3O_4/MnO_2 nanocomposite is a promising non-noble metal oxygen catalyst with improved catalytic performance for ORR. Table 4 shows that the assessment of electrochemical characteristics of recently investigated MnO_2 based electrocatalysts. Hence, the surface are the as-prepared Co_3O_4/MnO_2 composite (193.37 m^2g^{-1}) is lower than

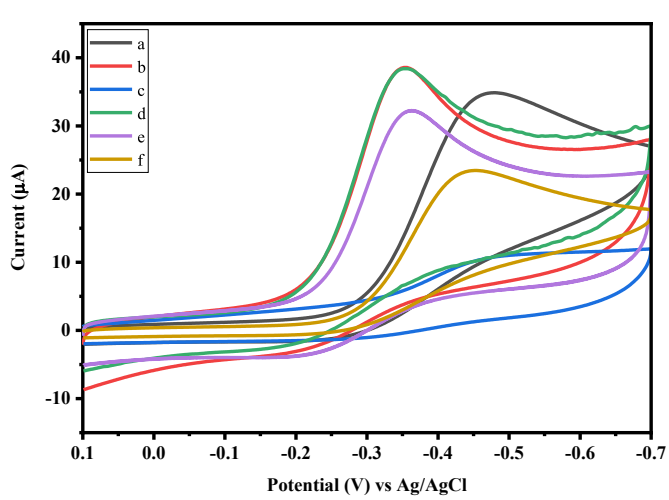

Figure 12. CV pattern of modified electrodes of (a) MnO_2 in O_2-saturated, (b) Co_3O_4/MnO_2-1-1 O_2-saturated, (c) Co_3O_4/MnO_2-1-1 in N_2-saturated, (d) Co_3O_4/MnO_2-1-2 in O_2-saturated, (e) Co_3O_4/MnO_2-1-5 in O_2-saturated, and (f) Co_3O_4 in O_2-saturated solution of KOH (0.1 M) with 50 mV s^{-1}scan rate.

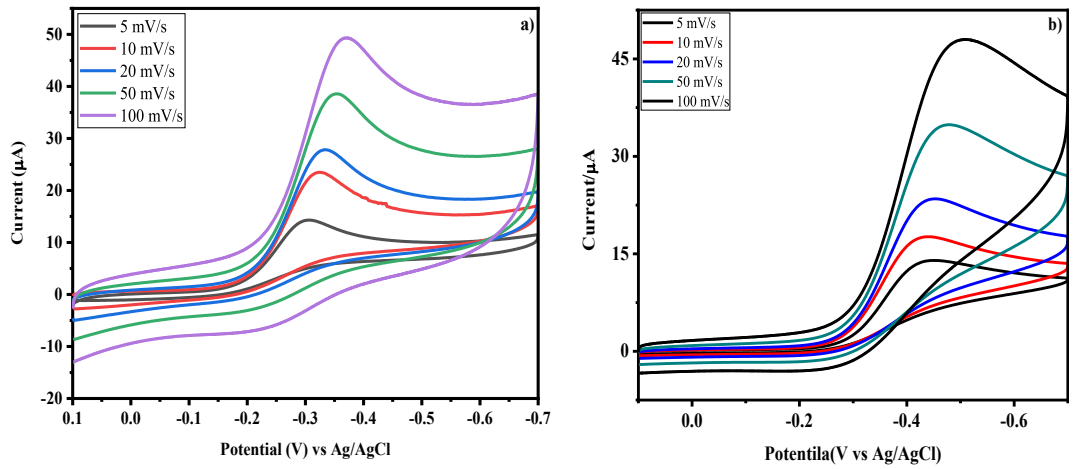

Figure 13. CV profile of (a) MnO_2 and (b) Co_3O_4/MnO_2-1-1 nanocomposite at various scan rates.

those of Ag–MnO_2/graphene composite (426.4 m^2g^{-1}) and α-MnO_2/Co_3O_4 (214.6 m^2g^{-1}), however the value of n is greater than that of Ni–MnO_2 nanoneedles ($n = 2.33$), and approximately equivalent with Pt/C, which shows that the improvement of the electrochemical activity of the Co_3O_4/MnO_2 composite.

3.9.4. Electrochemical active surface area (ECSA) analysis

The ECSA of a catalyst is a vital performance indicator of electrochemical reaction; hence, CV of Co_3O_4, MnO_2 and Co_3O_4/MnO_2 nanocomposite synthesized catalysts are evaluated by ECSA in oxygen-saturated KOH (0.1 M) aqueous electrolyte at 50 mVs^{-1} [82]. Figure 16 shows the reduction peak current of Co_3O_4, MnO_2, and Co_3O_4/MnO_2 nanocomposite. The peak current (I_p) increment of Co_3O_4/MnO_2 in the observed CV curve related to an irreversible two-electron transfer process using the synthesized nanomaterials as electron mediators in modified electrodes in 0.1 M KOH solution. The peak current corresponding to the reduction of Co_3O_4/MnO_2 nanocomposite increases with the interaction effect of Co_3O_4 and MnO_2. Thus, Randles-Sevcik technique (equation 20) was applied to calculate the ECSA of as-prepared electrodes [83].

$$I_p = 268600n^{3/2}\,AD^{1/2}\,Cv^{1/2} \tag{20}$$

where A is the ECSA of the electrode (cm^2), C is the concentration of oxygen in the aqueous solution ($C = 1.2 \times 10^{-6}$ mol L^{-1}), Ip (A) is the peak current, D is the diffusion coefficient of oxygen in 0.1 M KOH solution (1.9×10^{-5} m^2 s^{-1}), n is the number of electrons transferred, and v (V/s) is the scan rate for this calculation is 50 mV/s. The ECSA values were 1.24×10^{-3}, 8.3×10^{-4}, and 1.38×10^{-3} cm^2 for MnO_2, Co_3O_4, and Co_3O_4/MnO_2 nanocomposite modified electrodes, correspondingly (Table 5) [84]. Therefore, the larger ECSA of Co_3O_4/MnO_2/GCE results the higher double layer capacitance of Co_3O_4/MnO_2/GCE as compared to Co_3O_4 and MnO_2 electrodes.

4. Conclusions

In summary, MnO_2 and Co_3O_4/MnO_2 nanocomposites were developed by using a co-precipitation approach. The effect of molar ratio of Mn/Co in physicochemical characteristics and catalytic activity of the as-prepared materials were investigated. The electrocatalytic characteristics of as-synthesized nanomaterials were studied in 0.1 KOH alkaline media by LSV and CV test. The physicochemical and electrochemical characteristics were studied using SEM, FTIR, BET, XRD, TGA/DTA, ICP-OES and UV-Vis. The XRD result shows that a complex tunnel, hexagonal, cubic and tetragonal structure of MnO_2 NPs and MnO_2/Co_3O_4 nanocomposites with an average crystallite size of 2.24–5.89 nm. Moreover, the XRD analysis confirmed that Co_3O_4 integration with MnO_2 at different molar ratios promotes α, β, and γ-MnO_2 formation. The morphological analysis shows that MnO_2 NPs has spherical-like nanoflowers which are made of many thin nanosheets, while Co_3O_4/MnO_2 with aggregated needle-like structures. The optical band gap of MnO_2, Co_3O_4/MnO_2-1-5, and Co_3O_4/MnO_2-1-1 nanocomposites were 3.07 eV 2.6 eV, and 2.3 eV, respectively. FTIR studies confirmed the formation of M-O spectra (M = Co, Mn) in the as-prepared NPs. The thermal examinations through TGA/DTA show that a MnO_2/Co_3O_4 nanocomposites was thermally stable associated with Co_3O_4 and MnO_2 nanoparticles. The electrochemical behaviors were analyzed via LSV and CV test for Co_3O_4, MnO_2 and MnO_2/Co_3O_4 nanocomposites. The result shows that an improved catalytic activity to ORR was obtained for the as-prepared Co_3O_4/MnO_2 nanocomposites in an alkaline condition. Thus, Co_3O_4/MnO_2 electrocatalyst with mass ratio of 1:1 showed high catalytic activity to ORR because of the synergistic effect of Co_3O_4 and MnO_2 nanoparticles. Therefore, MnO_2/Co_3O_4 nanocomposites describe highly effective, eco-friendly, durable, and cost-effective ORR electrocatalyst, which may be used in fuel cells or metal-air batteries under alkaline conditions.

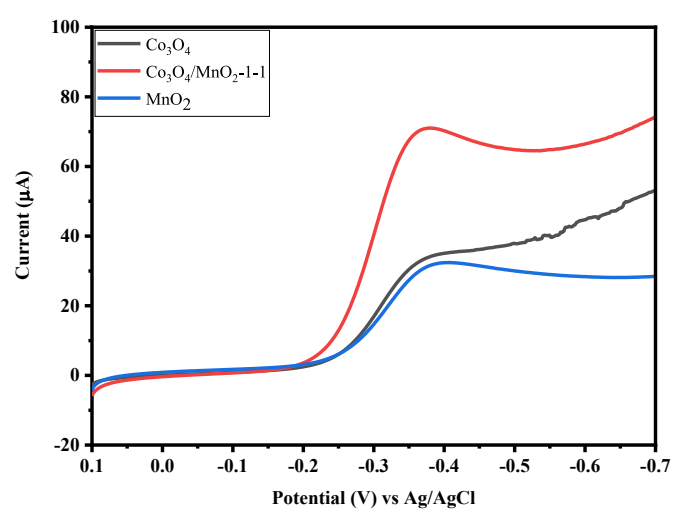

Figure 14. LSV plot of Co_3O_4, MnO_2 and Co_3O_4/MnO_2 nanocomposites at 5 mVs^{-1} scan rates.

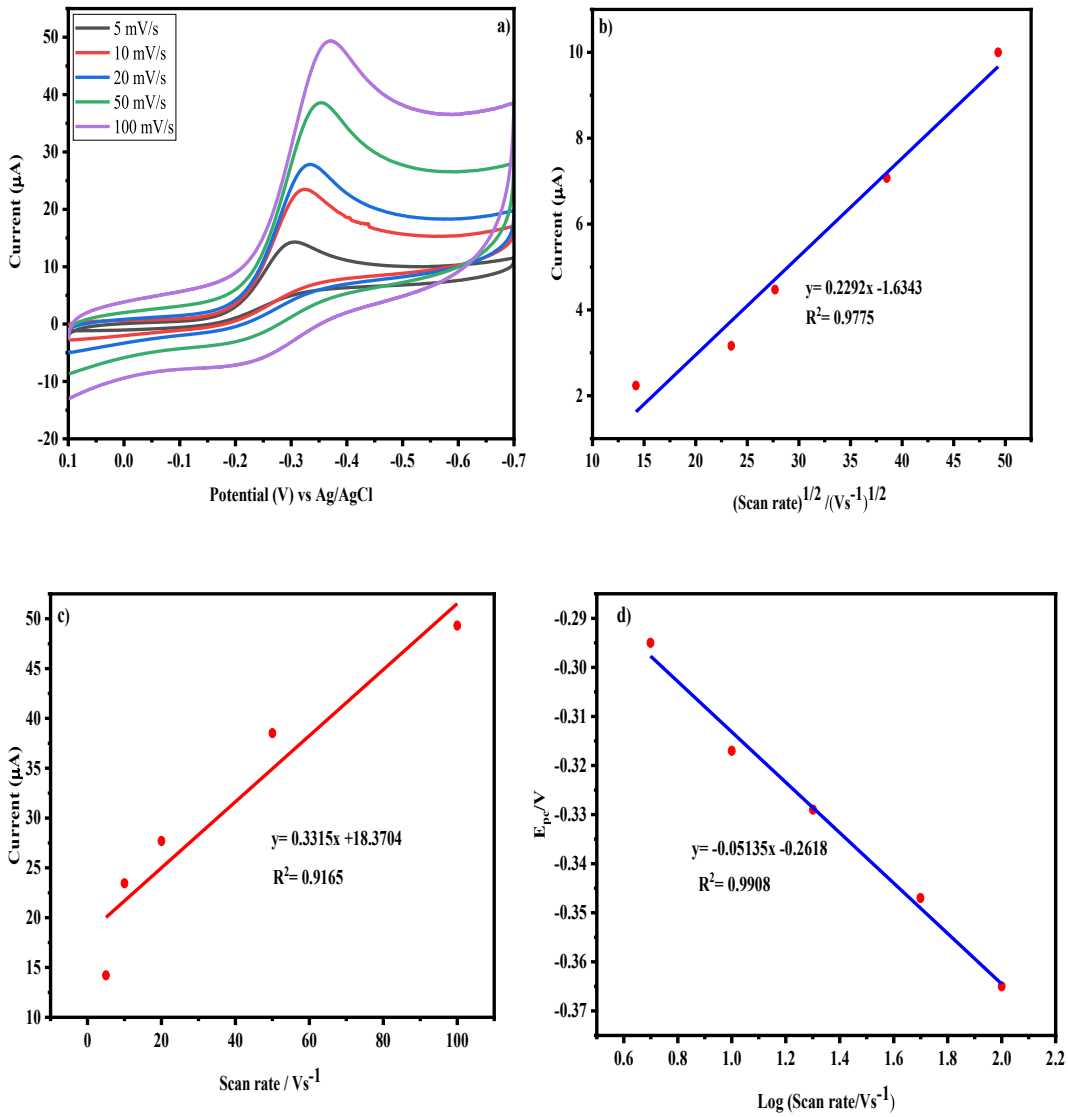

Figure 15. (a) The CV patterns of GC modified Co_3O_4/MnO_2-1-1 electrode with several scan rates. (b) Scheme of cathodic peak current vs. $v^{1/2}$. (c) Scheme of cathodic peak current vs. v. (d) Scheme of E_{pc} vs. log v.

Table 4. Comparison of recent research reports showing the ORR electrochemical properties of various MnO_2 based electrocatalysts.

Active electrode Material	Synthesis Method	Morphology	Electrolyte	Surface area (m^2g^{-1})	Electrochemical property	n	Ref.
Co_3O_4/MnO_2 composite	Co-precipitation	Needle-like structure	0.1 M KOH	193.37	Shows the ORR potential (V) at -0.352 V (vs. Ag/AgCl)	3.7	This work
Ag–MnO_2/graphene composite	Immersion-calcination	Nanoparticles	0.1 M KOH	426.4	Onset potential of 0.068 V and ORR reaction limiting current density of 5.62 mA cm^{-2}	3.9	[77]
α-MnO_2 and Co_3O_4	One-step solution-based	Microspheres & nanoparticulate	0.1 M KOH	214.6	Half-wave potential and potential of -0.197 and -0.226 V (vs. Ag/AgCl) at -3 mA cm^{-2}	3.94	[78]
Pt/C	-	Amorphous	0.1 M KOH	-	Shows current density of 5.02 J/mA cm^{-2}	3.89	[79]
PVP- MnO_2/CNT	Hydrothermal	Aggregates Nanoparticles	0.1 M of aqueous Na_2SO_4	-	Shows the ORR potential (V) at -0.43 (vs. Ag/AgCl)	-	[80]
MnO_2/rGO	Electrodeposition	Yarn-rod shape	0.1 M KOH	50.5	Shows the ORR potential (V) at -0.36 V	3.92	[79]
Ni–MnO_2 nanoneedles	Hydrothermal	Nanoneedle	0.1 M KOH	-	Shows the current densities of -1.24 mA cm^{-2} with a reduction potentials of -0.43 V	2.33	[81]

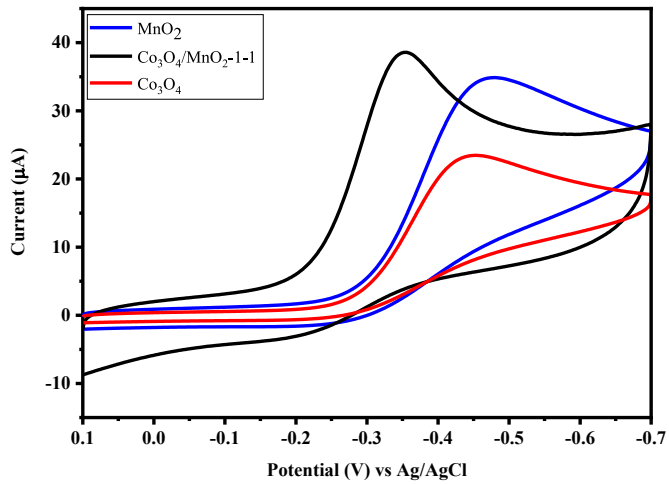

Figure 16. CV pattern of Co_3O_4, MnO_2, and Co_3O_4/MnO_2 nanocomposite modified electrodes in 0.1 M KOH solution by applying 50 mVs^{-1}.

Table 5. ECSA values for different catalysts computed via Randles-Sevcik equation.

No.	Catalyst	ECS Area (cm^2)
1	Co_3O_4 NPs	8.3 x 10^{-4}
2	MnO_2 NPs	1.24 x 10^{-3}
3	Co_3O_4/MnO_2-1-1 nanocomposite	1.38 x 10^{-3}

Declarations

Author contribution statement

Ababay Ketema Worku: Conceived and designed the experiments; Performed the experiments; Analyzed and interpreted the data; Wrote the paper.

Delele Worku Ayele, Nigus Gabbiye Habtu: Analyzed and interpreted the data; Contributed reagents, materials, analysis tools or data; Wrote the paper.

Temesgen Atnafu Yemata: Conceived and designed the experiments; Performed the experiments; Wrote the paper.

Funding statement

This work was supported by Bahir Dar Institute of Technology, Bahir Dar University, Ethiopia.

Data availability statement

Data will be made available on request.

Declaration of interests statement

The authors declare no conflict of interest.

Additional information

No additional information is available for this paper.

References

[1] H. Chen, Y. Li, H. Liu, Q. Ji, L. Zou, J. Gao, Metal-organic framework-derived sulfur and nitrogen dual-doped bimetallic carbon nanotubes as electrocatalysts for oxygen evolution reaction, J. Solid State Chem. 288 (2020) 121421.
[2] C. Liu, R. Tian, D. Sun, H. Liu, H. Duan, MOF-derived 3D hollow porous carbon/graphene composites for advanced lithium-ion battery anodes, J. Solid State Chem. 290 (2020) 121568.
[3] Y. Liu, S.P. Jiang, Z. Shao, Intercalation pseudocapacitance in electrochemical energy storage: recent advances in fundamental understanding and materials development, Mater. Today Adv. 7 (2020) 100072.
[4] K.O. Oyedotun, M.J. Madito, D.Y. Momodu, A.A. Mirghni, T.M. Masikhwa, N. Manyala, Synthesis of ternary NiCo-MnO2 nanocomposite and its application as a novel high energy supercapattery device, Chem. Eng. J. 335 (2018) 416–433.
[5] H. Gao, Y. Liu, Y. Ma, E. Meng, Y. Zhang, Synthesis of N-doped Co@C/CNT materials based on ZIF-67 and their electrocatalytic performance for oxygen reduction, Ionics (Kiel) (2021).
[6] H. Salari, M. Kohantorabi, Facile template-free synthesis of new α-MnO2 nanorod/silver iodide p–n junction nanocomposites with high photocatalytic performance, New J. Chem. 44 (2020) 7401–7411.
[7] M.-Y. Chung, C.-T. Lo, High-performance binder-free RuO2/electrospun carbon fiber for supercapacitor electrodes, Electrochim. Acta 364 (2020) 137324.
[8] C.-S. Liu, C.-L. Huang, H.-C. Fang, K.-Y. Hung, C.-A. Su, Y.-Y. Li, MnO2-based carbon nanofiber cable for supercapacitor applications, J. Energy Stor. 33 (2021) 102130.
[9] N. Palaniyandy, M.A. Kebede, K. Raju, K.I. Ozoemena, L. le Roux, M.K. Mathe, R. Jayaprakasam, $α$-MnO2 nanorod/onion-like carbon composite cathode material for aqueous zinc-ion battery, Mater. Chem. Phys. 230 (2019) 258–266.
[10] A.K. Worku, D.W. Ayele, N.G. Habtu, Recent advances and future perspectives in engineering of bifunctional electrocatalysts for rechargeable zinc–air batteries, Mater. Today Adv. 9 (2021) 100116.
[11] Y. Chuminjak, P. Singjai, A. Tuantranont, C. Sriprachuabwong, A. Wisitsoraat, High-capacity charge storage electrodes based on nickel oxide and nickel–cobalt double hydroxide nanocomposites on 3D nickel foam prepared by sparking and electrodeposition, J. Alloys Compd. 841 (2020) 155793.
[12] Q. Zhou, M. Zeng, X. Wu, Y. Zhang, G. Qin, Hierarchically porous core-shell microspheres assembled from Mn2O3/TiO2 nanoparticles for enhanced lithium storage, J. Alloys Compd. 786 (2019) 368–376.
[13] Z. Li, Z. Liu, B. Li, D. Li, Z. Liu, H. Wang, Q. Li, Large area synthesis of well-dispersed β-MnO2 nanorods and their electrochemical supercapacitive performances, J. Taiwan Inst. Chem. Eng. 65 (2016) 544–551.
[14] N. Ma, S. Kosasang, A. Krittayavathananon, N. Phattharasupakun, S. Sethuraman, M. Sawangphruk, Effect of intercalated alkali ions in layered manganese oxide nanosheets as neutral electrochemical capacitors, Chem. Commun. 55 (2019) 1213–1216.
[15] J. Kang, M. Hwang, K. Seong, L. Lyu, D. Ko, Y. Piao, Three-dimensional nanocomposite of graphene/MWCNT hydrogel grafted with Ni–Co hydroxide nanorods as high-performance electrode for asymmetric supercapacitor, Electrochim. Acta 346 (2020) 136258.
[16] F. Ochai-Ejeh, M.J. Madito, K. Makgopa, M.N. Rantho, O. Olaniyan, N. Manyala, Electrochemical performance of hybrid supercapacitor device based on birnessite-type manganese oxide decorated on uncapped carbon nanotubes and porous activated carbon nanostructures, Electrochim. Acta 289 (2018) 363–375.
[17] C. Wang, X. Li, Q. Li, H. Pang, Graphene/Co 3 O 4 composites in application of electrochemical energy conversion and storage, FlatChem 16 (2019) 100107.
[18] Y. Li, Z. Li, L. Lei, T. Lan, Y. Li, P. Li, X. Lin, R. Liu, Z. Huang, X. Fen, Y. Ma, Chemical vapor deposition-grown carbon nanotubes/graphene hybrids for electrochemical energy storage and conversion, FlatChem 15 (2019) 100091.
[19] T.N. Myasoedova, M.N. Grigoryev, T.S. Mikhailova, Effect of nickel and manganese doping on the structure, morphology and the electrochemical performance of the silicon-carbon films, J. Alloys Compd. 855 (2021) 157504.
[20] Y. Kumar, S. Chopra, A. Gupta, Y. Kumar, S.J. Uke, S.P. Mardikar, Low temperature synthesis of MnO2 nanostructures for supercapacitor application, Mater. Sci. Energy Technol. 3 (2020) 566–574.
[21] K. Qian, Z. Qian, Q. Hua, Z. Jiang, W. Huang, Structure-activity relationship of CuO/MnO 2 catalysts in CO oxidation, Appl. Surf. Sci. 273 (2013) 357–363.
[22] K. Xu, W. Li, Q. Liu, B. Li, X. Liu, L. An, Z. Chen, R. Zou, J. Hu, Hierarchical mesoporous NiCo2O4@MnO2 core–shell nanowire arrays on nickel foam for aqueous asymmetric supercapacitors, J. Mater. Chem. A. 2 (2014) 4795–4802.
[23] H. Chen, X.Y. Liu, X.D. Hao, Y.X. Zhang, Facile biphasic synthesis of TiO2–MnO2 nanocomposites for photocatalysis, Ceram. Int. 42 (2016) 19425–19428.
[24] M.Y. Rafiq, F. Iqbal, F. Aslam, M. Bilal, N. Munir, I. Sultana, F. Ashraf, F. Manzoor, N. Hassan, A. Razaq, Fabrication and characterization of ZnO/MnO2 and ZnO/TiO2 flexible nanocomposites for energy storage applications, J. Alloys Compd. 729 (2017) 1072–1078.
[25] B. Liu, Y. Zhang, J. Wang, M. Lu, Z. Peng, G. Li, T. Jiang, Investigations on the MnO2-Fe2O3 system roasted in air atmosphere, Adv. Powder Technol. 28 (2017) 2167–2176.
[26] X. Li, N. Xu, H. Li, M. Wang, L. Zhang, J. Qiao, 3D hollow sphere Co3O4/MnO2-CNTs: its high-performance bi-functional cathode catalysis and application in rechargeable zinc-air battery, Green Energy Environ. 2 (2) (2017) 316–328.
[27] Q. Miao, Y. Du, G. Wang, Z. Sun, Y. Zhao, S. Zhang, In situ generated 3D hierarchical Co3O4@MnO2 core–shell hybrid materials: self-assembled fabrication {,} morphological control and energy applications, J. Mater. Chem. A. 7 (2019) 5967–5980.
[28] H. Zhao, W. Guo, Coordinated control method of multiple hybrid energy storage systems based on distributed event-triggered mechanism, Int. J. Electr. Power Energy Syst. 127 (2021) 106637.
[29] M. Chen, Q. Cheng, Y. Qian, J. He, X. Dong, Alkali cation incorporated MnO2 cathode and carbon cloth anode for flexible aqueous supercapacitor with high wide-voltage and power density, Electrochim. Acta 342 (2020) 136046.
[30] F. Raza, X. Ni, J. Wang, S. Liu, Z. Jiang, C. Liu, H. Chen, A. Farooq, A. Ju, Ultrathin honeycomb-like MnO2 on hollow carbon nanofiber networks as binder-free electrode for flexible symmetric all-solid-state supercapacitors, J. Energy Stor. 30 (2020) 101467.

[31] X. Zhang, T. Wang, C. Jiang, F. Zhang, W. Li, Y. Tang, Manganese dioxide/cabon nanotubes composite with optimized microstructure via room temperature solution approach for high performance lithium-ion battery anodes, Electrochim. Acta 187 (2016) 465–472.
[32] A. Xia, W. Yu, J. Yi, G. Tan, H. Ren, C. Liu, Synthesis of porous δ-MnO2 nanosheets and their supercapacitor performance, J. Electroanal. Chem. 839 (2019) 25–31.
[33] H.Z. Chi, Y.Q. Wu, Y.K. Shen, C. Zhang, Q. Xiong, H. Qin, Electrodepositing manganese oxide into a graphene hydrogel to fabricate an asymmetric supercapacitor, Electrochim. Acta 289 (2018) 158–167.
[34] G. Liu, L. Ma, Q. Liu, The preparation of Co3O4@MnO2 hierarchical nano-sheets for high-output potential supercapacitors, Electrochim. Acta 364 (2020) 137265.
[35] J. Qi, Y. Zhu, J. Zhang, M. Jiao, C. Wang, Synthesis of porous hollow six-branched star-like MnO and its enhanced electrochemical properties as a lithium ion anode material, Ceram. Int. 46 (2020) 20878–20884.
[36] R.A. Davoglio, G. Cabello, J.F. Marco, S.R. Biaggio, Synthesis and characterization of α-MnO2 nanoneedles for electrochemical supercapacitors, Electrochim. Acta 261 (2018) 428–435.
[37] L. Liu, Y. Luo, W. Tan, Y. Zhang, F. Liu, G. Qiu, Facile synthesis of birnessite-type manganese oxide nanoparticles as supercapacitor electrode materials, J. Colloid Interface Sci. 482 (2016) 183–192.
[38] P. Zhao, N. Wang, M. Yao, H. Ren, W. Hu, Hydrothermal electrodeposition incorporated with CVD-polymerisation to tune PPy@MnO2 interlinked core-shell nanowires on carbon fabric for flexible solid-state asymmetric supercapacitors, Chem. Eng. J. 380 (2020) 122488.
[39] B. Wang, J. Qiu, H. Feng, N. Wang, E. Sakai, T. Komiyama, Preparation of MnO2/carbon nanowires composites for supercapacitors, Electrochim. Acta 212 (2016) 710–721.
[40] M. Zhang, D. Yang, J. Li, Effective improvement of electrochemical performance of electrodeposited MnO2 and MnO2/reduced graphene oxide supercapacitor materials by alcohol pretreatment, J. Energy Stor. 30 (2020) 101511.
[41] W. Xiao, W. Zhou, H. Yu, Y. Pu, Y. Zhang, C. Hu, Template synthesis of hierarchical mesoporous δ-MnO2 hollow microspheres as electrode material for high-performance symmetric supercapacitor, Electrochim. Acta 264 (2018) 1–11.
[42] R.-B. Li, L.-L. Yu, S. Li, J. Fan, R. Luo, J.-T. Zhao, Facile synthesis of hierarchical mesoporous beta-manganese dioxide nanoflowers with extremely high specific surface areas for high-performance electrochemical capacitors, Electrochim. Acta 284 (2018) 52–59.
[43] J. Lv, Y. Zhang, Z. Lv, X. Huang, Z. Wang, X. Zhu, B. Wei, Strontium doped lanthanum manganite/manganese dioxide composite electrode for supercapacitor with enhanced rate capability, Electrochim. Acta 222 (2016) 1585–1591.
[44] A.A. Chaugule, V.S. Mane, H.A. Bandal, H. Kim, A.S. Kumbhar, Ionic liquid-derived Co3O4-N/S-doped carbon catalysts for the enhanced water oxidation, ACS Sustain. Chem. Eng. 7 (2019) 14889–14898.
[45] S.E. Seo, S.H. Choi, Preparation of the nanostructured radioisotope metallic oxide by neutron irradiation for use as radiotracers, Appl. Sci. 7 (2017).
[46] E. Arciga-Duran, Y. Meas, J.J. Pérez-Bueno, J.C. Ballesteros, G. Trejo, Electrochemical synthesis of Co 3 O 4-x films for their application as oxygen evolution reaction electrocatalysts: role of oxygen vacancies, J. Electrochem. Soc. 165 (2018) H3178–H3186.
[47] P. Iamprasertkun, C. Tanggarnjanavalukul, A. Krittayavathananon, J. Khuntilo, N. Chanlek, P. Kidkhunthod, M. Sawangphruk, Insight into charge storage mechanisms of layered MnO2 nanosheets for supercapacitor electrodes: in situ electrochemical X-ray absorption spectroscopy, Electrochim. Acta 249 (2017) 26–32.
[48] N. Zhang, G. Guo, B. He, J. Zhu, J. Wu, J. Qiu, Synthesis and research of MnO2–NiO composite as lithium-ion battery anode using spent Zn–Mn batteries as manganese source, J. Alloys Compd. 838 (2020) 155578.
[49] R.M. Obodo, E.O. Onah, H.E. Nsude, A. Agbogu, A.C. Nwanya, I. Ahmad, T. Zhao, P.M. Ejikeme, M. Maaza, F.I. Ezema, Performance evaluation of graphene oxide based Co3O4@GO, MnO2@GO and Co3O4/MnO2@GO electrodes for supercapacitors, Electroanalysis 32 (2020) 2786–2794.
[50] B. Li, X. Zhang, J. Dou, P. Zhang, Construction of MnO2@NH4MnF3 core-shell nanorods for asymmetric supercapacitor, Electrochim. Acta 347 (2020) 136257.
[51] X. Han, F. Cheng, C. Chen, F. Li, J. Chen, A Co3O4@MnO2/Ni nanocomposite as a carbon- and binder-free cathode for rechargeable Li–O2 batteries, Inorg. Chem. Front. 3 (2016) 866–871.
[52] M. Huang, X.L. Zhao, F. Li, W. Li, B. Zhang, Y.X. Zhang, Synthesis of Co3O4/SnO2@MnO2 core-shell nanostructures for high-performance supercapacitors, J. Mater. Chem. A. 3 (2015) 12852–12857.
[53] S. Ramesh, K. Karuppasamy, H.S. Kim, H.S. Kim, J.H. Kim, Hierarchical Flowerlike 3D nanostructure of Co3O4@MnO2/N-doped Graphene oxide (NGO) hybrid composite for a high-performance supercapacitor, Sci. Rep. 8 (2018) 1–12.
[54] X. Li, F. Dong, N. Xu, T. Zhang, K. Li, J. Qiao, Co3O4/MnO2/Hierarchically porous carbon as superior bifunctional electrodes for liquid and all-solid-state rechargeable zinc–air batteries, ACS Appl. Mater. Interfaces 10 (2018) 15591–15601.
[55] M. Ma, Y. Yang, Y. Chen, F. Wu, W. Li, P. Lyu, Y. Ma, W. Tan, W. Huang, Synthesis of hollow flower-like Fe3O4/MnO2/Mn3O4 magnetically separable microspheres with valence heterostructure for dye degradation, Catalysts 9 (2019).
[56] M. Feng, G. Zhang, Q. Du, L. Su, Z. Ma, X. Qin, G. Shao, Co3O4@MnO2 core shell arrays on nickel foam with excellent electrochemical performance for aqueous asymmetric supercapacitor, Ionics (Kiel) 23 (2017) 1637–1643.
[57] R. Rajagopal, K.-S. Ryu, Morphologically engineered cactus-like MnO2 nanostructure as a high-performance electrode material for energy-storage applications, J. Energy Stor. 32 (2020) 101880.
[58] D.J. Tarimo, K.O. Oyedotun, A.A. Mirghni, B. Mutuma, N.F. Sylla, P. Murovhi, N. Manyala, Enhanced electrochemical performance of supercapattery derived from sulphur-reduced graphene oxide/cobalt oxide composite and activated carbon from peanut shells, Int. J. Hydrogen Energy 45 (2020) 33059–33075.
[59] R.M. Al-Tuwirqi, A.A. Al-Ghamdi, F. Al-Hazmi, F. Alnowaiser, A.A. Al-Ghamdi, N.A. Aal, F. El-Tantawy, Synthesis and physical properties of mixed Co3O4/CoO nanorods by microwave hydrothermal technique, Superlattice. Microst. 50 (2011) 437–448.
[60] R.S. Reena, A. Aslinjensipriya, M. Jose, S.J. Das, Investigation on structural, optical and electrical nature of pure and Cr-incorporated cobalt oxide nanoparticles prepared via co-precipitation method for photocatalytic activity of methylene blue dye, J. Mater. Sci. Mater. Electron. 31 (2020) 22057–22074.
[61] T. Li, J. Gao, P. Fu, C. Zhe, S. Wang, Z. Lin, The preparation and ozone-sensing performance of Co 3 O 4 nanobricks, J. Mater. Sci. Mater. Electron. 30 (2019) 9678–9682.
[62] L. Chen, Q. Zhang, H. Xu, X. Hou, L. Xuan, Y. Jiang, Y. Yuan, Amorphous 3D nanoflake array-assembled porous 2D cobalt–oxalate coordination polymer thin sheets with excellent pseudocapacitive performance, J. Mater. Chem. A 3 (2015) 1847–1852.
[63] A.M. Hashem, H.M. Abuzeid, D. Mikhailova, H. Ehrenberg, A. Mauger, C.M. Julien, Structural and electrochemical properties of α-MnO2 doped with cobalt, J. Mater. Sci. 47 (2012) 2479–2485.
[64] Y. Jin, L. Wang, Y. Shang, J. Gao, J. Li, Q. Jiang, X. Du, C. Ji, X. He, Characterization of porous micro-/nanostructured Co3O4 microellipsoids, Electrochim. Acta 188 (2016) 40–47.
[65] Y. Haoran, D. Lifang, L. Tao, C. Yong, Hydrothermal synthesis of nanostructured manganese oxide as cathodic catalyst in a microbial fuel cell fed with leachate, Sci. World J. 2014 (2014).
[66] C. Wu, Y. Zhu, M. Ding, C. Jia, K. Zhang, Fabrication of plate-like MnO2 with excellent cycle stability for supercapacitor electrodes, Electrochim. Acta 291 (2018) 249–255.
[67] L. Kang, M. Zhang, J. Zhang, S. Liu, N. Zhang, W. Yao, Y. Ye, C. Luo, Z. Gong, C. Wang, X. Zhou, X. Wu, S.C. Jun, Dual-defect surface engineering of bimetallic sulfide nanotubes towards flexible asymmetric solid-state supercapacitors, J. Mater. Chem. A. 8 (2020) 24053–24064.
[68] A.K. Worku, D.W. Ayele, N.G. Habtu, M.A. Teshager, Z.G. Workineh, Recent progress in MnO2-based oxygen electrocatalysts for rechargeable zinc-air batteries, Mater. Today Sustain. 13 (2021) 100072.
[69] D.U. Lee, P. Xu, Z.P. Cano, A.G. Kashkooli, M.G. Park, Z. Chen, Recent progress and perspectives on bi-functional oxygen electrocatalysts for advanced rechargeable metal-air batteries, J. Mater. Chem. A 4 (2016) 7107–7134.
[70] D.U. Lee, P. Xu, Z.P. Cano, A.G. Kashkooli, M.G. Park, Z. Chen, Recent progress and perspectives on bi-functional oxygen electrocatalysts for advanced rechargeable metal–air batteries, J. Mater. Chem. A 4 (2016) 7107–7134.
[71] M. Dupont, A.F. Hollenkamp, S.W. Donne, Electrochemically active surface area effects on the performance of manganese dioxide for electrochemical capacitor applications, Electrochim. Acta 104 (2013) 140–147.
[72] A. Ashok, A. Kumar, M.A. Matin, F. Tarlochan, Synthesis of highly efficient bifunctional Ag/Co3O4 catalyst for oxygen reduction and oxygen evolution reactions in alkaline medium, ACS Omega 3 (2018) 7745–7756.
[73] H.H. Hamzah, N.N. Ahmad Kamal, M. Meneghello, S.A. Shafiee, T. Sönmez, M.N.A. Mohamad Taib, S.H. Mohd Samsuri, M.F. Meor Zulkifli, Hexanediamine monolayer electrografted at glassy carbon electrodes enhances oxygen reduction reaction in aqueous neutral media, J. Electrochem. Soc. 167 (2020) 166508.
[74] A.K. Worku, D.W. Ayele, N.G. Habtu, M.A. Teshager, Z.G. Workineh, Enhancing oxygen reduction reaction activity of ε-MnO2 nanoparticles via iron doping, J. Phys. Chem. Solid. 157 (2021) 110207.
[75] J.I. Gowda, S.T. Nandibewoor, Electrochemical behavior of paclitaxel and its determination at glassy carbon electrode, Asian J. Pharm. Sci. 9 (2014) 42–49.
[76] A.K. Worku, D.W. Ayele, N.G. Habtu, Influence of nickel doping on MnO2 nanoflowers as electrocatalyst for oxygen reduction reaction, SN Appl. Sci. 3 (2021).
[77] S. Liu, X. Qin, Preparation of a Ag-MnO2/graphene composite for the oxygen reduction reaction in alkaline solution, RSC Adv. 5 (2015) 15627–15633.
[78] M.F. Fink, J. Eckhardt, P. Khadke, T. Gerdes, C. Roth, Bifunctional α-MnO2 and Co3O4 catalyst for oxygen electrocatalysis in alkaline solution, ChemElectroChem 7 (2020) 4822–4836.
[79] B. Huang, X. Zhang, J. Cai, W. Liu, S. Lin, A novel MnO2/rGO composite prepared by electrodeposition as a non-noble metal electrocatalyst for ORR, J. Appl. Electrochem. 49 (2019) 767–777.
[80] H.R. Ong, C.W. Woon, M.S. Ahmad, A. Yousuf, C.K. Cheng, M.M.R. Khan, Facile synthesis of PVP-MnO2/CNT composites as ORR electrocatalyst for an air-cathode microbial fuel cell, Int. J. Electrochem. Sci. 13 (2018) 7789–7799.
[81] J. Hao, Y. Liu, H. Shen, W. Li, J. Li, Y. Li, Q. Chen, Effect of nickel-ion doping in MnO2 nanoneedles as electrocatalyst for the oxygen reduction reaction Effect of nickel-ion doping in MnO 2 nanoneedles as electrocatalyst for the oxygen reduction reaction, J. Mater. Sci. Mater. Electron. (2016).
[82] P. Zhu, Y. Zhao, Cyclic voltammetry measurements of electroactive surface area of porous nickel: peak current and peak charge methods and diffusion layer effect, Mater. Chem. Phys. 233 (2019) 60–67.
[83] P. Connor, J. Schuch, B. Kaiser, W. Jaegermann, The determination of electrochemical active surface area and specific capacity revisited for the system MnOx as an oxygen evolution catalyst, Zeitschrift Fur Phys. Chemie. 234 (2020) 979–994.
[84] S. Zhao, H. Yu, R. Maric, N. Danilovic, C.B. Capuano, K.E. Ayers, W.E. Mustain, Calculating the electrochemically active surface area of iridium oxide in operating proton exchange membrane electrolyzers, J. Electrochem. Soc. 162 (2015) F1292–F1298.